SINGLE PIXEL NEUTRON CAMERA USING COMPRESSIVE SENSING

A Thesis

by

YURIY JACOB AYZMAN

Submitted to the Office of Graduate and Professional Studies of
Texas A&M University
in partial fulfillment of the requirements for the degree of

MASTER OF SCIENCE

Chair of Committee,	Ryan G McClarren
Committee Members,	Raytcho Lazarov
	Craig Marianno
Head of Department,	Yassin A Hassan

May 2016

Major Subject: Nuclear Engineering

ABSTRACT

The ability to quickly and cheaply localize radiation sources is incredibly important in the national security field. The ever increasing amount of intercontinental shipping makes cargo containers a likely vector for the transfer of prohibited material. Current methodology for detection of neutron sources suffers from size and expense limitations. The single pixel neutron camera offers a simple design that is inexpensive to implement allowing for an increase in detection points. The compressive sensing framework provides fast and accurate localization of sources among surrounding shielded material. Additionally, this design frees the detector from volume restrictions allowing for increased detection efficiency. This makes finding weak sources more likely. Finally, the focus is shifted from detector to collimator design, which is generally simpler and has fewer restrictions.

Using MCNP numerical simulations, various source geometries were imaged and localized. The collimator featured a simple, multiplex type design that allows taking measurements at each individual pixel location. The ability of a compressive sensing based device was proven to achieve the objectives outlined above. Additionally, the simulations of the design show that sources can be localized using $\sim 5\%$ sampling rate. This means fast and accurate identification of sources even in heavily shielded containers. Single pixel neutron detection devices are shown to be ideal for cheap and durable course spatial detection.

TABLE OF CONTENTS

Page

LIST OF FIGURES

FIGURE Page

LIST OF TABLES

TABLE Page

1. INTRODUCTION: NEUTRON IMAGING AND COMPRESSIVE SENSING

Source localization within large, shielded volumes is a problem of great importance in the nuclear security field. Over 90% of shipping is currently being accomplished via cargo containers[1]. The containers offer a large volume within which dangerous or illegal materials can be hidden[1]. The difficulty in detecting this material comes from the fact that other items in the container can be positioned to shield targets from detection. This leads to an increased threat for transfer of undesirable materials.

Neutron imaging is ideal to resolve this problem because interrogation techniques are designed to identify the inner structure of some target and neutrons typically interact well with the materials of interest in nuclear security. Current systems can be extremely fragile and expensive. They have limits on the neutron energies to which they are sensitive. Additionally, the fine temporal and spatial resolution of some modern digital systems may be unnecessary in situations where only the position of the material needs to be identified.

The single pixel compressive sensing methodology has been developed for exactly this scenario. It allows for a single detector to build a 2D image from a series of samples. This will reduce the dependence on expensive detector arrays and can allow for more flexible detection of various neutron energies. The second part is especially important because it allows for better classifications of the material.

1.1 Neutron Imaging

The process of imaging neutrons has significant benefits and a long history. Neutrons interact with the nuclei making them complementary to x-ray based imaging.

The neutron particle has a neutral charge meaning it is not affected by electrical fields, thus making its presence difficult to detect directly. The same property allows it to penetrate further into material. This being the case, a nuclear reaction must be induced giving off products that can be measured. A long standing method for accomplishing this was film, which had a metallic layer, that converted neutrons to a detectable form of radiation[2]. Typical materials found in more modern detectors include Boron-10, Gadolinium, Lithium-6, and other strong absorbers[2]. The basic imaging system is laid out below.

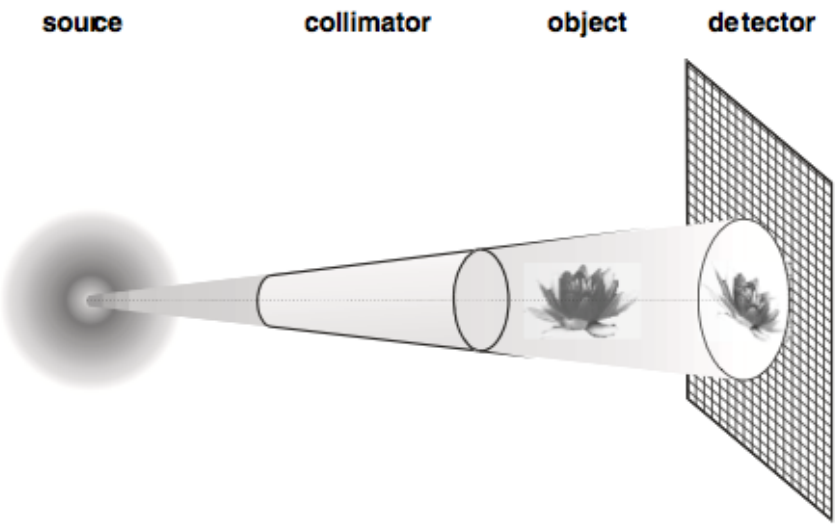

Figure 1.1: Typical setup for neutron imaging system[3]

The source puts out a stream of neutrons, which may have some distribution in energy and direction. Since detectors are generally tuned to detect a specific energy range and the angular distribution will add blur, the neutrons must be collimated.

The collimator simply rejects all the undesirable neutrons, allowing a stream perpendicular to the target object. The neutrons then pass through the object being imaged, interacting through scattering or absorption reactions. The detected image is given as a shadow of the neutrons with only the neutrons able to make it through being counted.

An alternative case is when the target and source are one and the same. In this case the neutrons are simply collimated and detected allowing for the source to be localized. This is useful when a neutron source is surrounded by shielding material and the goal is to identify its location.

State of the art methods for imaging neutrons involve CCD cameras, imaging plates, silicon flat panels, and pixel detectors[2]. These methods possess high spatial resolution but have difficulty detecting high-energy neutrons. The detection areas are on the order of $100\,\mathrm{cm}^2$ so these methods are not ideal for large scale imaging without significant cost[2]. As neutron energy increases, the detection volume experiences limitations on how much it can be shrunk. This is primarily because neutral particles will travel further prior to interacting. The very high-energy neutrons needed for some methods need extremely large volumes to be detected.

Neutron imaging can be broken down into two categories: passive and active interrogation. Passive interrogation means that detection is focused on the neutrons given of by the target. This is the method used for detecting radioactive sources which emit neutron particles. Active interrogation is performed by transmitting a neutron flux through the target and measuring the shielding properties. This is a good way to measure density differences and to check the hydrogen content of the target. Ac-

tive interrogation also gives the ability to select neuron energy, which determines the interaction cross-sections.

These cross-sections will determine the type of interactions that occur within the target material and therefore will decide which characteristics are displayed. For example, fissile material can have a higher probability of interaction at lower energies but the higher energy neutrons have a higher fission neutron yield. Also hydrogen rich materials will have a high likelihood of scattering meaning that items surrounded by hydrogen can be difficult to image. These characteristics are problem specific and can be tweaked to obtain the desired information.

Neutron detection systems typically have three measures of quality. These measures are spatial resolution, time resolution, and image quality[2]. The spatial resolution is related to how detailed an individual image can be. The time resolution determines how quickly an image can be obtained. The image quality is a description of the signal to noise ratio. The compressive sensing methodology will allow the time resolution to be sacrificed for spatial resolution and image quality. This is primarily useful for allowing a simple neutron detector with no spatial resolution to be able to construct a 2D image by taking a series of samples. As the number of samples increases, the image quality and available spatial resolution also increase. The increase in sampling time lowers the time resolution of the detector.

1.2 Compressive Sensing

In recent years there has been significant interest in the compressed sensing field[4]. This relatively new field allows for sampling at rates lower than the Shannon-Nyquist rate of two times the bandwidth[4]. This means that a data set of N elements can be

restored from K < N samples. The ability to restore data with fewer samples is due to the exploitation of structure. The Shannon-Nyquist theorem does not assume that the data has any structure therefore the limit is a theoretical maximum[4]. Since most data does have structure, that structure can be exploited in order to reduce the sampling rate.

The primary structure that is exploited by compressed sensing is sparsity in some basis[4]. This means that the data can be represented using a basis that has fewer degrees of freedom than the original basis. The sparsity structure is used to create operators and reconstruction algorithms. These algorithms allow for the recovery of sparse data from an underdetermined system. Solving an optimization problem, whose goal is to minimize the solution in a norm while minimizing complexity, typically does this.

The other piece of the data reconstruction is the sampling method. The sampling must be incoherent with the sparsity basis. For this reason, random sampling is commonly used due its incoherent nature. Sampling is achieved by randomly mapping the basis to obtain the sample elements. With these sample values and the random map the signal can be reconstructed.

The basis to create a single pixel neutron camera is obtained from the work performed by Duarte et al. The members of the digital signals processing group at Rice university created a single pixel light camera using lens components, a digital micromirror device (DMD), a photodiode, and an analog to digital converter (ADC)[5]. One lens focuses the scene onto the DMD, which then allows for random linear maps of the scene to be captured by the photodiode via the second lens[5]. The ADC

then converts the voltage sensed by the photodiode to a digital signal. This process produces one sample and is repeated for different random maps on the DMD, generating a vector of voltage values. The scene is then reconstructed using Total Variation (TV) minimization via the l1magic software suite[5].

1.3 New Work

In order to improve current detection methods, compressive sensing techniques can be applied to neutron imaging platforms. The improvements lie in effectively utilizing large detection areas. The image producing neutrons are collimated into a beam that then hits the detector array. The neutrons incident on the detection surface produce a single integrated value. This result has no spatial dependence regardless of the surface dimensions. This will lead to blur in the image reducing the spatial resolution.

An alternative approach is to collect a random map of neutron incident on the detection surface. Although this also yields a single integrated value, as multiple random samples are collected an image can be reconstructed. The random maps are controlled by the collimator passing and blocking neutrons in spatial coordinates. The resolution of this image will depend solely on the collimator dimensions and the sampling time will depend on source strength coupled with image complexity.

This approach allows for simple and inexpensive detectors to be used for identifying materials inside a volume. The ability to use larger detectors means greater efficiency and less noise. This becomes important when imaging heavily shielded targets since very few neutrons will penetrate so it is important to capture as many as possible. Passive systems can scan both living and inanimate targets in order to identify

radioactive sources. Active systems can be used to find non-neutron emitting but still hazardous items in inanimate targets. The methodology is versatile and easily adapted to multiple uses because it primarily deals with the collimator design. Detection is especially effective if it is needed to quickly identify neutron emitters within simple geometries containing limited hydrogen material.

2. THEORY

Image reconstruction in the single pixel camera is accomplished by solving a variant of the l_1 minimization problem. This takes the form of minimizing the gradient of the pixels while constraining the solution by the inner products of the image and a random map. The reason l_1 minimization works is due to the shape of the norms. The l_p norms have the following form:

$$\|x\|_p = \left(\sum_{i=1}^{N} x_i^p \right)^{1/p} . \tag{2.1}$$

It is important to note that for $p < 1$ the above definition does not satisfy the triangle inequality, which is one of the requirements for a norm[6]. Also, the norm given when $p = 0$ is defined as the number of nonzero elements in the vector x. On the unit circle the norms for the various p values form the geometric shapes depicted in Figure 2.1.

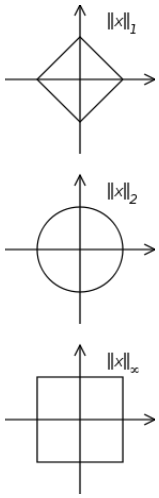

Figure 2.1: Various l_p norms shown in $\mathbb{R}^2$

For l_p norms, as p increases the error in estimating some value becomes spread out among the coefficients[6]. This is because the intersection of a line with the shape will give an estimate, whose minimum distance from the actual value becomes larger with p and will fall between the axes. This makes the estimated coefficients sparse for the l_1 norm but not for the higher p norms[6]. The way the estimates fall on the norms is graphically shown in Figure 2.2.

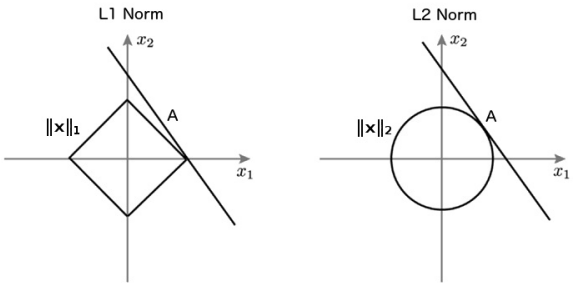

Figure 2.2: Estimation of variables ($x1$, $x2$) in $\mathbb{R}^2$ using l_1 and l_2 norms

The line A is able to provide an estimate in l_1 that is sparse in the two coefficients x_1 and x_2. This is due to the anisotropic nature of the l_1 norm. Conversely, the l_2 norm more evenly distributes the estimate between the two coefficients. This lack of sparsity is why the l_2 norm and higher p norms are not suited for reconstruction.

With this logic, the l_0 norm allows for the sparsest possible reconstruction of data. Unfortunately, l_0 minimization problems are np hard so l_1 minimization is the next best choice. The above figure shows that the l_1 norm will provide sparse solutions and a good approximation of the l_0 norm. With the satisfaction of some properties with regard to the problem, it can be shown that $l_0 = l_1$ with a high degree of

probability.

2.1 Compressive Sensing Theory

The compressive sensing framework differs from a regular camera in that instead of measuring pixels the camera measures a series of inner products between the scene and some test function[5]. The inner product in this case is the sum of an element-wise multiplication of two vectors. The image, which is located in $\mathbb{R}^N$ space, is reconstructed using K measurements where $K < N$. This is possible because the image structure can be exploited. A common structure type in the case of images is sparsity, meaning that pixel values can be represented with some $m < N$ coefficients. This is the basis for image compression. The test functions are random maps since the random basis is incoherent with most fixed basis to a high degree of probability[7].

The image reconstruction problem is presented as a matrix A operating on some image x to give a set of measurements b that have lower dimensionality than the original. This can be written as,

$$Ax = b. \tag{2.2}$$

In order to guarantee that l_1 minimization will yield recovery of the desired set of coefficients the vector x must have certain properties. These properties describe the behavior of the system Ax and prove that a unique solution exists, this solution is the sparsest, and the l_1 solution is the equivalent of the l_0 solution.

Sparsity and incoherent sampling are the two properties that guarantee these results. Still this result is not applicable to all A matrices or all m-sparse x vectors[8]. The applicability of these guarantees depends on the support of x as well as its sign se-

quence. It has been shown that if x has a fixed support perfect recovery via l_1 can be achieved for an "overwhelming majority" of sign sequences[8].

2.1.1 Sparsity

Sparsity plays a key role in ability to reconstruct a compressed image. It is important to represent the image in the sparsest manner possible. The number of non-zero coefficents is directly related to the number of samples needed for recovery[8].

Since the image is likely sparse in some basis, the image vector x is decomposed into a series of coefficients and orthonormal vectors. An example of the sparsifying basis are wavelets. The wavelet coefficients are sparse for images with many of the values being close to zero. This being the case they can be discarded with little effect to reconstruction quality. The expansion is as follows:

$$x = \sum_{i=1}^{N} \alpha_i \psi_i, \tag{2.3}$$

where ψ_i is a single orthonormal vector and $\alpha_i =< x, \psi_i >$. The α coefficients can be described as m-sparse meaning there are m non-zero values. The operator $< \cdot, \cdot >$ represents the standard dot product.

The basis vectors are combined to from the sparsifying matrix, Ψ. This matrix is used to further decompose the problem to:

$$A'\alpha = b, \tag{2.4}$$

where $A' = \Phi\Psi$.

The Φ matrix is the sampling methodology for this design and is described in the sampling section. The end result is a sparse representation of the image using a series of coefficients that are then found through the solution of an optimization problem.

2.1.2 Incoherent Sampling

The camera design employed for neutron imaging is a multiplex type. The standard measurement style for these types of cameras is a raster scan[5]. This means that each pixel is sampled at a time with all the other collimator flaps shut. In this case the ϕ_m is a delta function. The raster scan time is equal to the detection time multiplied by the number of pixels. Compressive sensing handles this a little differently.

The sampling basis needs to be incoherent with the sparsity basis in order to reconstruct the image. Coherence is measured in the following way.

$$\mu(\Phi, \Psi) = \sqrt{n} \max_{1 \leq i,j \leq n} |< \phi_i, \psi_j >| \tag{2.5}$$

The value for coherence is shown as μ which is calculated as a function of the total number of pixels n and the inner product between the columns of the sampling and sparsifying basis.

It has been shown by Candes et al. that the number of samples required for reconstruction and the mutual coherence of the sampling and sparsifying basis has the following relationship.[8]

$$k \geq O(\mu^2(\Phi, \Psi) m \log(n)) \tag{2.6}$$

The number of samples required for reconstruction k is dependent on the mutual

coherence μ, number of non-zero elements m, and the total number of elements n. When this relationship is satisfied, the vector x is recovered by l_1 minimization to high probability.

Compressive sensing sampling sets ϕ_m to a random map of 0's and 1's. This map is achieved through the flap positions, where closed flaps correspond to a 0 and open flaps correspond to a 1. The sampling time for compressive sensing is the detection time multiplied by m, which is a number of samples much smaller than the pixel count. Mathematically this is shown in the following formulation:

$$b[m] = \langle \phi_m, x \rangle. \tag{2.7}$$

The combination of all the random maps build the sampling matrix, Φ. The fact that ϕ_m is a random map yields two positive properties. The measurements are robust meaning the loss of a single measurement will not significantly affect image quality[5]. The addition of measurements will progressively improve the reconstruction[5].

2.1.3 Convex Optimization

In mathematics, optimization problems are formulated to solve a minimization (or maximization) of a function under some constraints. The constraints can also be descriped as a series of functions, which define the region where the problem is feasible. This is shown as,

$$\begin{aligned} &\text{minimize } f_0(\mathbf{x}) \\ &\text{subject to } f_i(\mathbf{x}) \leq b_i, \;\; i = 1, \cdots, m. \end{aligned}$$

The function f_0 is called the objective function. This function and all the constraint functions, f_i, map the n dimensional vector $\mathbf{x}$ from $\mathbb{R}^n$ to $\mathbb{R}$. The value of f_0 evaluated at some solution $\mathbf{x} = \{x_1, \cdots, x_n\}$ is known as the objective value. The constraint functions are bounded by a corresponding constant, b_i. The values for each element of $\mathbf{x}$ can be bounded or unrestricted through the use of the constraint functions. The overall goal is to find an x that satisfies the constraints and minimizes the objective.

The various classes of optimization problems are defined based on the form of the objective and constraint functions[9]. For convex optimization, the functions, $f_i(\mathbf{x})$ for $i = 0, \cdots, m$ must satisfy

$$f_i(\alpha\mathbf{x} + \beta\mathbf{y}) \leq \alpha f(\mathbf{x}) + \beta f(\mathbf{y}). \tag{2.8}$$

The vectors **x,y** are contained in $\mathbb{R}^n$ while α, β are scalars such that $\alpha + \beta = 1$ and they are both nonnegative.

It is important to understand that in order for optimization problems to guarantee a solution certain conditions must be met. These conditions, called the Karush Kuhn Tucker (KKT) conditions, are assumed to be met. Additionally, the problems that are being solved are assumed to have feasible solutions. These assumptions are valid since this class of problems has been show to be feasible under the conditions required by this design[10].

2.1.3.1 Total Variation Minimization

A subclass of convex optimization problems, this technique minimizes a discrete gradient in a 2D matrix making it useful for image reconstruction[10].

Mathematically, the total variation is described as:

$$\mathrm{TV}(x) := \sum_{ij} \sqrt{(D_{h;ij}x)^2 + (D_{v;ij}x)^2} = \sum_{ij} \|D_{ij}x\|_2, \tag{2.9}$$

where the gradient is given as:

$$D_{h;ij}x = \begin{cases} x_{i+1,j} - x_{ij}, & i < n \\ 0, & i = n \end{cases}, \qquad D_{v;ij}x = \begin{cases} x_{i,j+1} - x_{ij}, & j < n \\ 0, & j = n \end{cases}.$$

The minimization problem used for restoring the image data attempts to find the smallest possible variation subject to the l_2 norm of the difference between the estimate and the observed data being less than some prescribed amount. This is shown as:

$$\min \mathrm{TV}(x) \text{ subject to } \|Ax - b\|_2 \leq \epsilon. \tag{2.10}$$

The A matrix is a linear map from the actual image x to the vector of observations, b. The error ϵ is the maximum allowed deviation between the solution iterations. This methodology is ideal for the imaging case because it takes into account the variation in two dimensions. Since images are two-dimensional signals they can be accurately represented in this problem.

This problem can be reformulated as a second-order cone program (SOCP) and therefore can be solved using standard interior point methods[10]. In l1magic the TV problems are solved by implementing a type of interior point method called the log-barrier algorithm.

Interior point methods are able to solve problems of the following form[9]

$$\begin{aligned} \text{minimize} \quad & f_0(\mathbf{x}) \\ \text{subject to} \quad & f_i(\mathbf{x}) \leq 0, \;\; i = 1, \cdots, m \\ & Ax = b \end{aligned}$$

where the f_i for $i = 0, \cdots, m$ are convex and twice differentiable. The matrix A must have a rank equal to the number of rows[9].

The log-barrier formulation transforms this problem by satisfying the f_i constraints through a penalty function.

$$\begin{aligned} \text{minimize} \quad & f_0(\mathbf{x}) + \sum_{i=1}^{m} I(f_i(x)) \\ \text{subject to} \quad & Ax = b \end{aligned}$$

The penalty function I has the following values for some constraint value.

$$I(u) = \begin{cases} 0, & u \leq 0 \\ \infty, & u > 0 \end{cases}$$

For the log-barrier method, $I(u) = (-1/\tau)\log(-u)$ is the commonly used approximation for the penalty function[9]. This function satisfies the desired constraint values and maintains the convexity of the problem. Now lets look at how the f_0 and f_i functions are formulated.

The standard TV_2 problem re-written in SOCP form has the following structure:

$$\min_z \langle c_0, z\rangle \quad \text{subject to } A_0 z = b$$
$$f_i(z) \leq 0, \;\; i = 1 \ldots n. \tag{2.11}$$

Each constraint, f_i, can be in one of two forms: linear, $f_i(z) = \langle c_i, z\rangle + d_i$ and second-order conic, $f_i(z) = \frac{1}{2}\left(\|A_i z\|_2^2 - (\langle c_i, z\rangle + d_i)^2\right)$.

Applying the general form to the problem at hand yields,

$$\min_{x,t} \sum_{ij} t_{ij} \quad \text{subject to} \quad \|D_{ij}\|_2 \leq t_{ij} \quad i, j = 1 \ldots n$$
$$\|Ax - b\|_2 \leq \epsilon. \tag{2.12}$$

The constraints for this problem can be rewritten by squaring both sides and subtracting the right hand side. This yields two constraint types:

$$f_{t_{ij}} = \frac{1}{2}(\|D_{ij}\|_2^2 - t_{ij}^2) \leq 0 \quad i, j = 1 \ldots n$$
$$f_\epsilon = \frac{1}{2}(\|Ax - b\|_2^2 - \epsilon^2) \leq 0.$$

Equation 2.12 is transformed into a set of unconstrained minimization problems that are solved through Newtons method[10]. Newtons method finds the direction of steepest decent for a quadratic norm and travels that path to find the optimal solution[9].

This is shown as:

$$\min_{x,t} \sum_{ij} t_{ij} + \frac{1}{\tau^{\kappa}} \sum_{i} -\log(-f) \tag{2.13}$$

In Eq. (2.13) the variable τ has the following property, $\tau^{\kappa} > \tau^{\kappa-1}$. This parameter also sets the accuracy of the estimation[9]. The inequality constraints are taken care of through a penalty function, which becomes infinite as the constraints are met or exceeded[10]. This can be clearly seen since as f approaches 0 the $\log(0) \to \infty$. As the iteration count, κ, increases the solution to Eq. (2.13), t^{κ}, approaches the solution to Eq. (2.12), t^{*}[10].

Each subproblem is solved using a few iterations of Newtons method with good accuracy and each following subproblem uses the solution to the previous problem as a starting point[10].

2.2 Error Analysis

The error analysis goal was to compare the number of samples taken to the quality of the reconstruction. The samples are random maps so it is possible for an image to get worse if the sample is a poor mapping of the space. Eventually, as the sample size increases the reconstruction error will drop.

In order to determine reconstruction quality, the mean squared error was used. This took the l_2 norm of the difference between the original image x and the reconstruction $\hat{x}$.

$$\epsilon = \frac{\|x - \hat{x}\|_2}{\|x\|_2} = \frac{\left(\sum_{i=1}^{N} (x_i - \hat{x}_i)^2\right)^{1/2}}{\left(\sum_{i=1}^{N} x_i^2\right)^{1/2}} \tag{2.14}$$

The error ϵ has the form of exponential decay as more samples are added. At some

number of samples less than or equal to the number of pixels in the image the error is zero.

The initial drop in error is large and than the error plateaus at some low level. This large drop will usually signal that most of the image is reconstructed properly.

3. CAMERA DESIGN

The ability to convert the single pixel theory to a real world device required the resolution of several engineering challenges. The source of the neutrons determines the material and detector requirements. The neutrons will be emitted at some energy. If the interrogation type is active than the designer can optimize the system to work with the neutrons that will provide desired object penetration. Conversely, a passive interrogation may have to deal with a wider range of energies requiring a different setup. For this process the system must be tuned to detect specific target materials. The source type also impacts the make up of the collimator. The collimation material must have high absorption to scattering cross-section ratio for neutrons. For lower energy neutrons materials like boron work, but for fast neutrons high-density materials provide the best attenuation. The collimator itself needs a way to provide spatially selective attenuation so that the random maps of neutrons can be detected. This was accomplished through a flap structure that can be expanded to provide shielding while maintaining spatial resolution. If the particle count is very low, collimator channels should be filled with a gas that has low interaction probability with neutrons so that they would not be deflected away from the detector.

3.1 Source and Problem Geometry

The source of neutrons in an imaging problem will typically determine much of the setup required. The design was tested with two source types: a 0.75 MeV isotropic source with various geometries and a 14 MeV plane source emitting neutron directly at the detection area. The various source configurations are shown in the table below. The 0.75 MeV source is indicative of typical fission/source neutron energies, which are in the 1 MeV range[11]. The geometries for the these sources were a Texas A&M

Case	Geometry	$W \times L \times H$ (cm)	Radius (cm)	Energy (MeV)
1	Texas A&M Logo	$100 \times 20 \times 60$	N/A	0.75
2a	Sphere	N/A	1	0.75
2b	Sphere	N/A	3	0.75
3	Plane	$256 \times 0 \times 256$	N/A	14.0

Table 3.1: Source configuration for various test cases

University logo surrounded by air and a spherical source in a cylinder of water. The logo was meant to test the imaging ability of the camera while the sphere was meant to check the ability to localize sources within shielding.

The 14.0 MeV source is a perpendicular plane that is used to penetrate the imaging target and determine composition. This is a type of active interrogation that uses highly penetrating neutrons to investigate the contents of a shipping container.

3.1.1 Case 1

The first problem looked at a Texas A&M logo shaped source made of air that isotropically emitted neutrons. The material was chosen to be air to avoid self-shielding and criticality considerations. The neutrons were emitted at 0.75 MeV. The collimator was modeled using borated polyethylene with a 32×32 grid of square channels all filled with ordinary air. This geometry shown in Figure 3.1 is meant to prove the ability of this detection scheme to image the source shape.

This logo is able to provide a complex source shape. This is important because the sources can be arranged in complex geometries. The geometric properties can be telling of the intent or danger associated with them. For instance, the likelihood of criticality can be analyzed by looking at the neutron energies emitted and the spatial

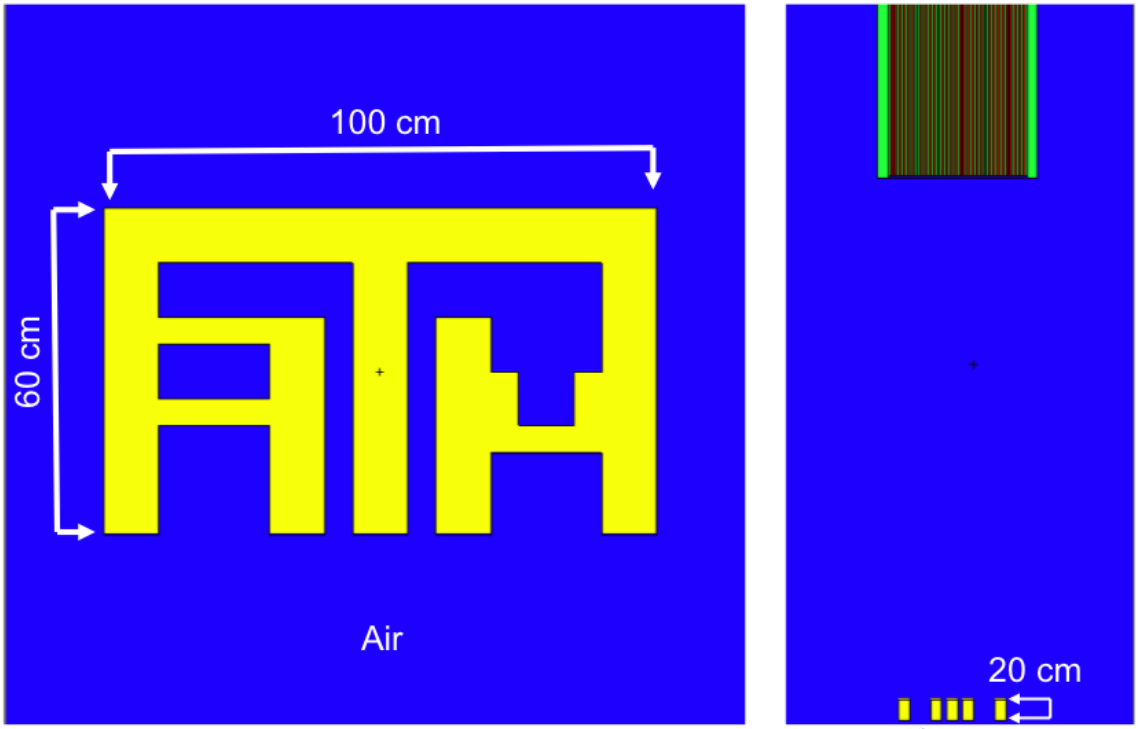

Figure 3.1: Texas A&M logo shaped, 0.75 MeV neutron source (a) front view (b) top down view

arrangement. This type of analysis goes hand in hand with isotopic composition studies.

3.1.2 Case 2a

Part one of the second problem looked at a spherical source made of air in a cylindrical drum of water. Water is a strong moderator of neutrons and therefore will make it more difficult to determine the source shape and location. The neutrons were again emitted isotropically at 0.75 MeV. The collimator remained unchanged from the previous problem. This problem is meant to show how detection is affected by strong scattering. Figure 3.2 show this below.

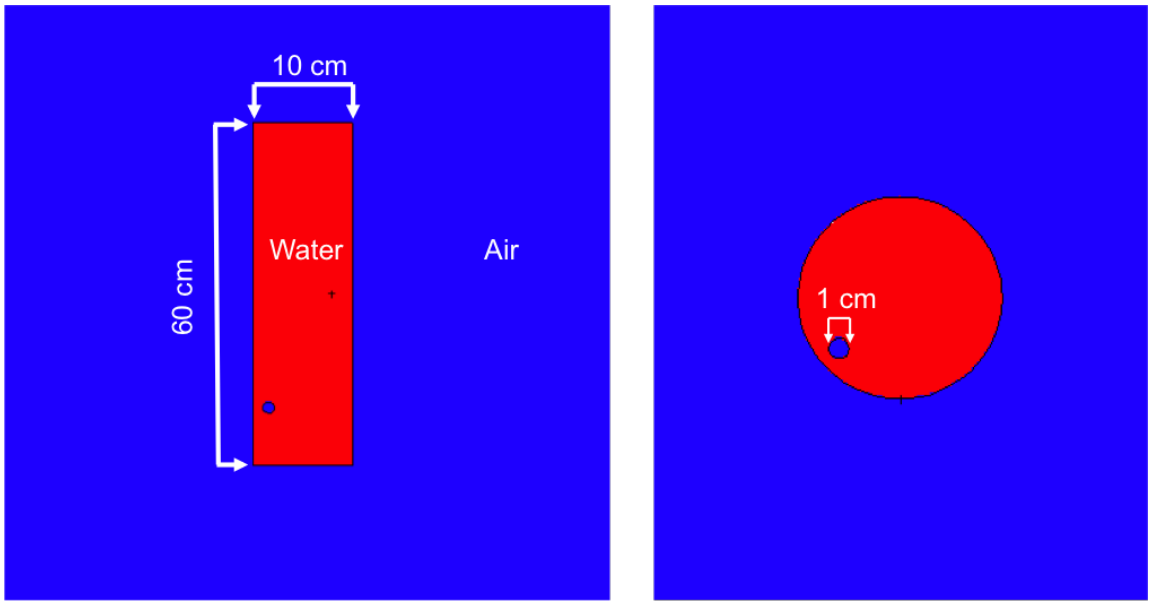

Figure 3.2: Smaller cylinder of H_2O with a spherical, 0.75 MeV neutron source (a) front view (b) top down view

The ability to localize a source surrounded by shielding material is important for finding hidden sources being transported past checkpoints. Once radiation is detected, this capability will help identify exactly where it is coming from.

3.1.3 Case 2b

Part two of the second problem increased the size of the cylinder and placed the source in a more shielded location. The increase in moderation made source detection more difficult. The source energies and collimator remained unchanged from the previous problem. This problem is meant to stress detection capabilities with regard to shielding. The setup is shown below in Figure 3.3.

Increasing shielding is important in order to gauge the affect it has on detection time and the ability to detect the source at all. This section allows the detector to be

pushed to the limit.

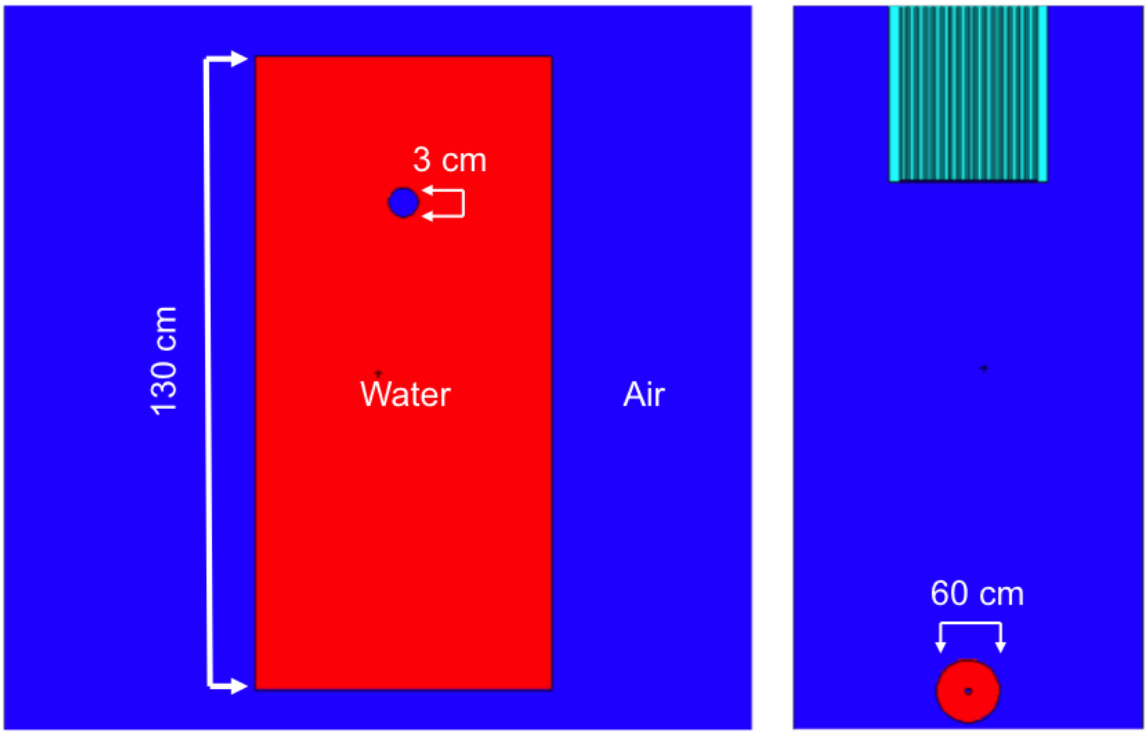

Figure 3.3: Larger cylinder of H_2O with a spherical, 0.75 MeV neutron source (a) front view (b) top down view

3.1.4 Case 3

The third problem looked at a plane source that emitted 14 MeV neutrons (typical in active interrogation) into the collimation direction. The neutrons pass through a shipping ULD loaded with a variety of shielding, radioactive, and explosive material. The collimator was modeled using densalloy (a high density shielding material) with a 64×64 grid of square channels all filled with ordinary air. The change in the collimator was due to the higher energy of neutrons. This problem geometry was

inspired by work being performed at Idaho National Laboratory (INL) and Commonwealth Science and Industrial Research Organisation (CSIRO) with regard to active interrogation[12][13]. This setup shown in the figure below is meant to demonstrate detection under active interrogation.

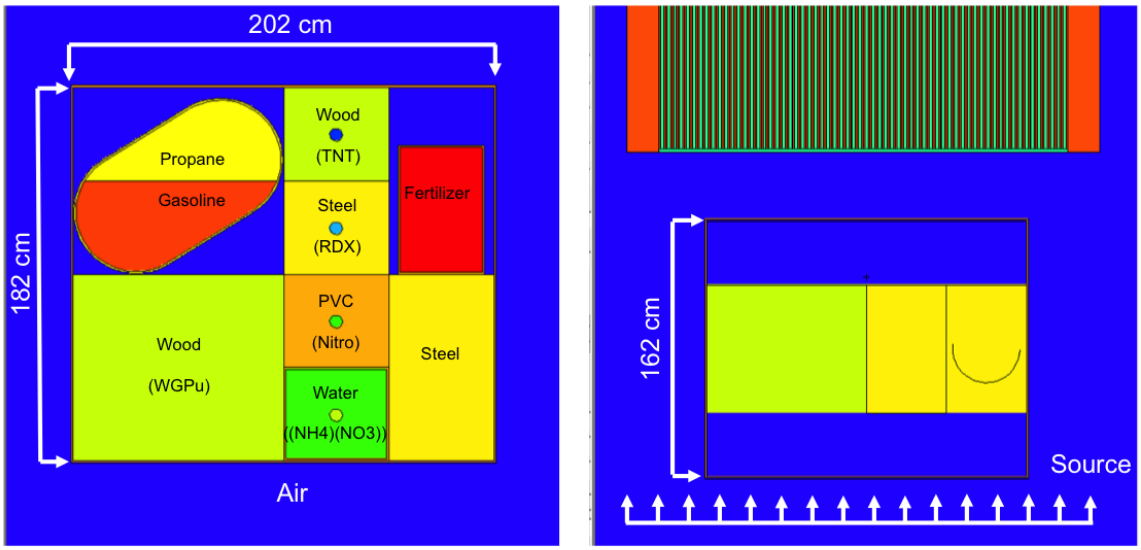

Figure 3.4: ULD containing radioactive and explosive material with various shields (a) front view (b) top down view

This test showed the density plots generated through the active interrogation of various material types. The highly scattering materials are extremely difficult to image while the organic materials provide good contrast. This will give an approximation of real world performance.

3.2 Collimator Materials and Geometry

The material make up of the collimator is important to provided the necessary shielding properties. The information on the configuration of the collimator for each prob-

lem is shown in table format below.

Case	Structure	Fill gas	Channel count
1	Borated Poly	Air	32×32
2a	Borated Poly	Air	32×32
2b	Borated Poly	Air	32×32
3	Densalloy	Air	64×64

Table 3.2: Collimator configuration for various test cases

The number of channels is increased for problem 3 since there are more objects to resolve. The slower neutrons are stopped using boron while the faster ones are shielded with tungsten. The fill gas used was air. An additional set of trials was run with helium fill gas, which is predicted to yield 4% more neutrons reaching the source per meter of collimator length[14]. This is relative to air that causes scattering and creates undesirable interactions.

The material selection is based on the cross-section data relative to neutron energy. The goal is to find the highest absorption cross-section for the energy of neutrons that the source emits. This will allow all neutrons that are not within the direction cone aimed at the collimator channels to be absorbed. If the neutrons scatter off the walls they can distort the image and lead to inaccurate results. Also, the absorption is important to reduce the background noise that exists when neutrons are detected in closed channels. Too much of this noise will require more samples and will interfere with the reconstruction algorithm. The plots generated using ENDF data are shown below.

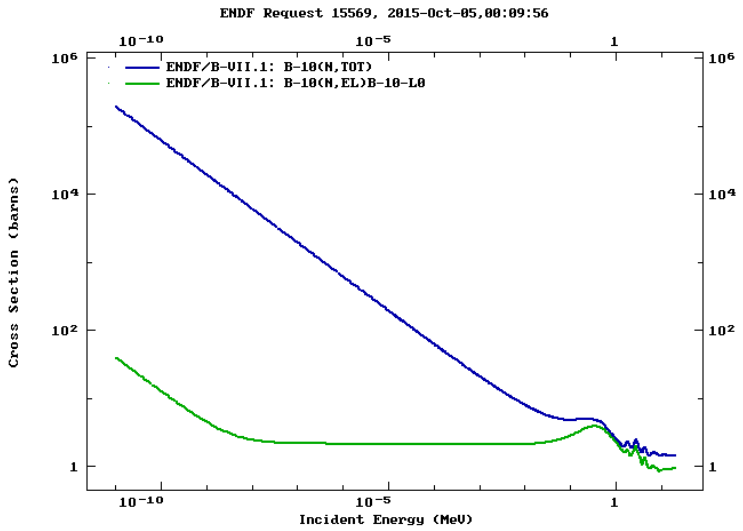

Figure 3.5: Boron-10 total and scattering cross-sections for neutron interactions

As can be seen, the boron-10 cross-section increases with decreasing energy making it a good collimating material for neutrons below 1 MeV.

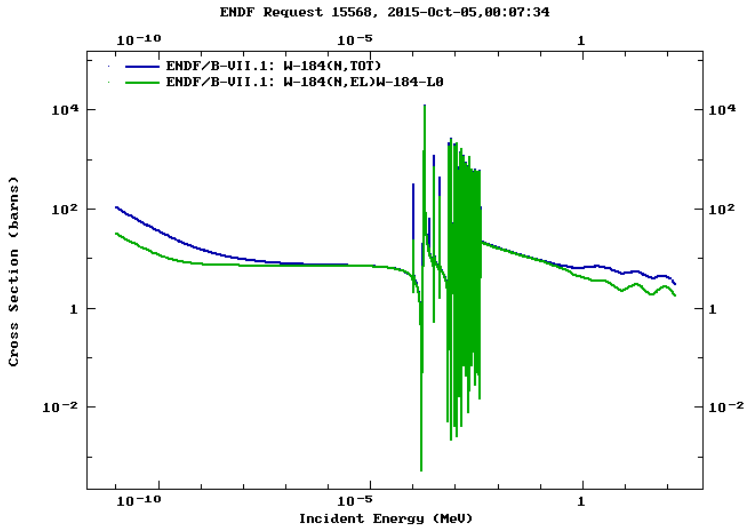

Figure 3.6: Tungsten-184 total and scattering cross-sections for neutron interactions

The main element of densalloy is tungsten. This cross-section provides better attenuation at 14 MeV than boron making it the material of choice for the very high energy neutrons.

The design of the Rice single pixel camera hinges on the ability of the DMD chip to reflect random subsets of the light from a scene on to a photodiode. Since neutrons cannot easily be reflected in this manner a special collimator design was created to replace the DMD.

The collimator would have absorbing flaps that can be opened or shut to create the same random subsets. When shut, the flaps would prevent neutrons from being detected and therefore contributing to the total reading. When open the neutrons would pass through freely and enter the detection space. This mimics the DMD mirror passing along light or deflecting it.

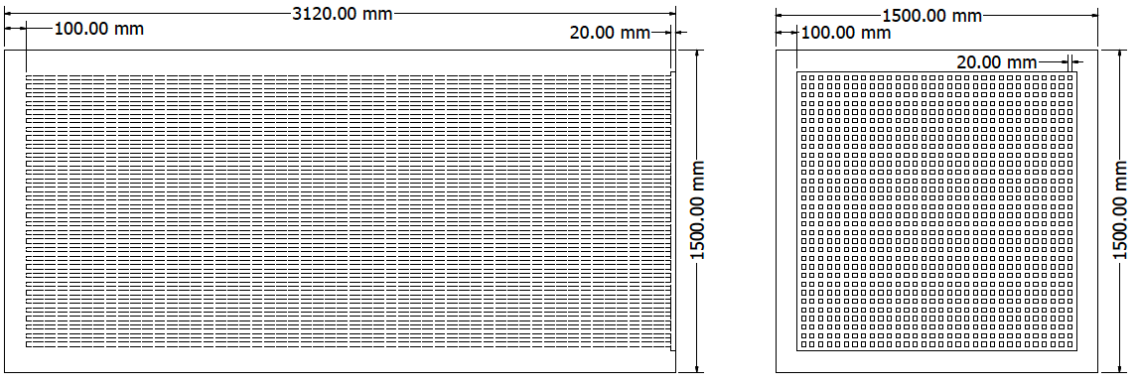

Figure 3.7: Dimensions for the first collimator

Figure 3.7 above and Figure 3.8 below show the composition and the dimensions of

the first collimator. This is a longer collimator with fewer channels. This design is used for cases 1, $2a$, and $2b$.

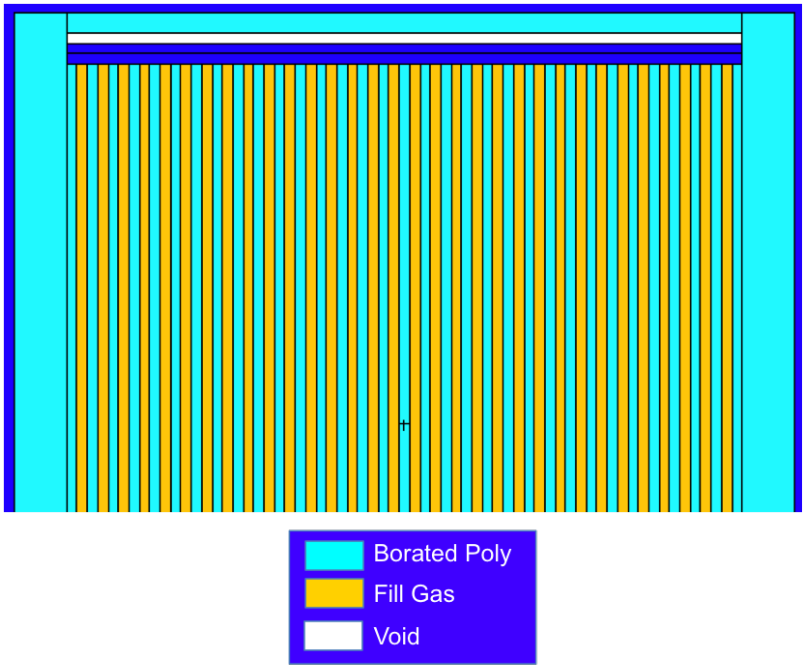

Figure 3.8: Materials for the first collimator

Figure 3.9 and Figure 3.10 below show the designs of the second collimator. This is a shorter collimator but has a much larger face with four times as many channels. This was done for better resolution. This design is used for case 3.

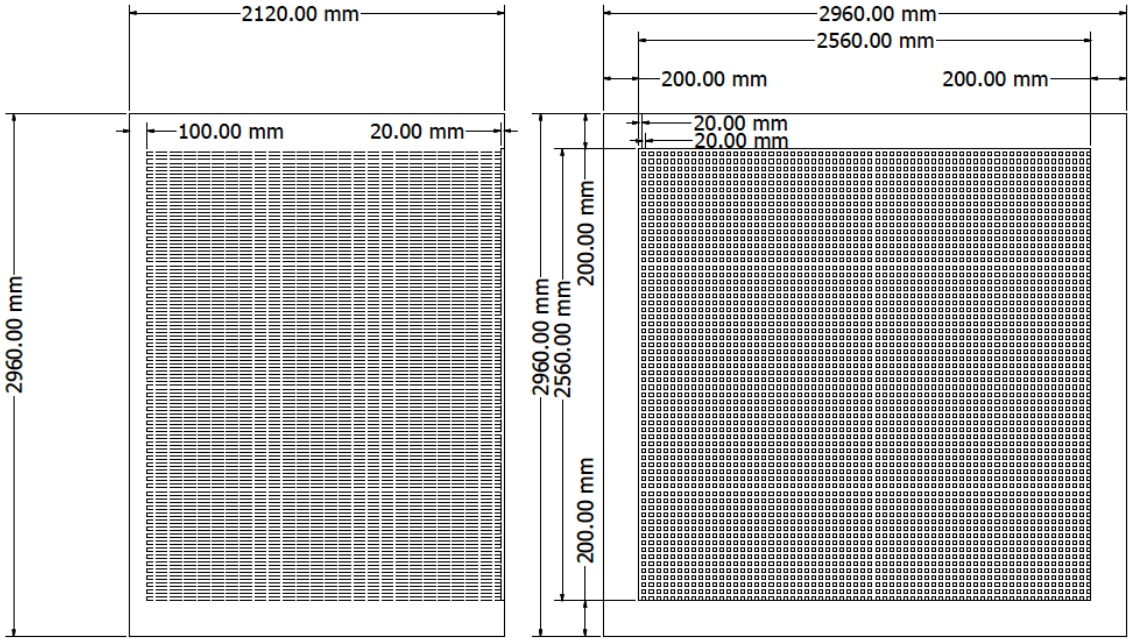

Figure 3.9: Dimensions for the second collimator

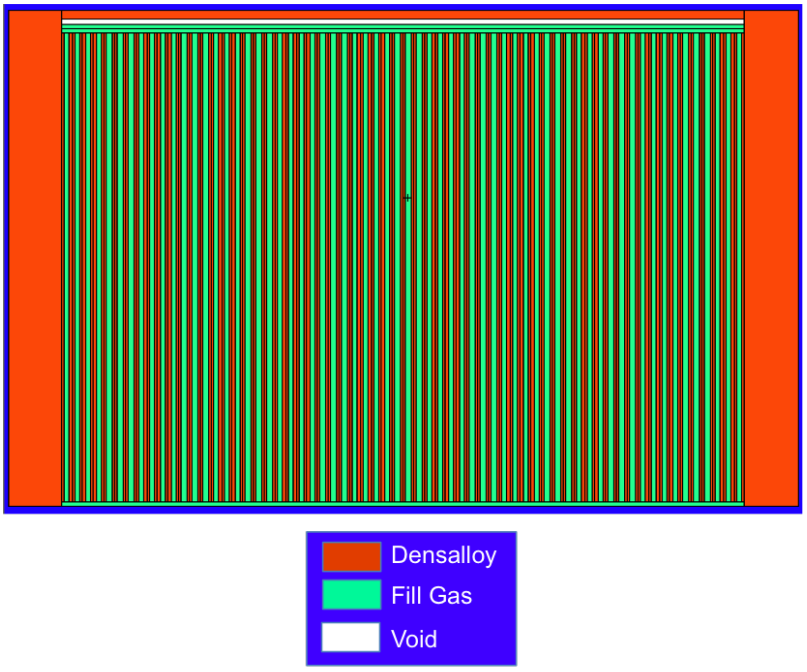

Figure 3.10: Materials for the second collimator

3.3 MCNP Simulations

Since the detection apparatus was not physically constructed, the various components had to be simulated computationally. The source, collimator, and detector portions were created in Monte Carlo N-Particle (MCNP) code. Three source problems were created to simulate different detection scenarios.

Case	Width (cm)	Length (cm)	Height (cm)	Fill
1	330	920	330	Air
2a	330	920	330	Air
2b	330	920	330	Air
3	660	620	660	Air

Table 3.3: Universe dimensions for the different cases

The problem only modeled neutron transport. This is because other particles can be shielded out and the health physics aspect was not something that this experiment encompassed. This simplification therefore should not alter real world results.

The detector was simulated with a void. This can be assumed to be accurate since the detector volume can be expanded until all neutrons that enter are captured without interfering with the design. The creation of a small void was done to reduce the problem size and reduce run time.

These problems were run once with all the collimator flaps simulated open. This yielded an FMESH (this is an MCNP mesh tally object) file that gave the neutron fluxes at the detector region across a grid of channels and wall areas. The grid data was parsed and uploaded into Matlab for manipulation. The code simulated detector

operations by creating an array of 2D random maps that are multiplied element-wise into the image and then summed to give a single sample value. The sample vector is generated at a preselected subsampling rate and the result is then restored using l1magic TV minimization solvers.

The noise was taken to be zero so that the data behind the closed flap was not counted. This perhaps gave better results than can be expected in real life but the flap thickness can be increased to provide this kind of shielding. Also, moderation can be applied to the neutrons so that only desired energies are allowed to enter the collimator thereby reducing noise. These are all design problems that can be looked at prior to construction.

4. RESULTS

The problems were run by taking the MCNP FMESH tally results and focusing on the values that penetrate the collimator channels. These images were sampled using various rates to observe the reconstruction quality and the l_2 error associated with the reconstruction. In many cases the images themselves are much more indicative of the effectiveness of the reconstruction. The l_2 error measures a sum of differences squared, which can be deceiving. The example of this is an image that has some localized values of 1 and 0's everywhere else. The reconstructions will display the position of the 1's but some of there pixels will be contained in the range $[0, 1]$. This will lead to some high value for l_2 error. Yet if the interest is localization the reconstruction is able to determine this even with high levels of error. For this reason a combination of l_2 error and the images themselves are used to judge the quality of reconstruction.

4.1 Case 1

The first case looks at a large source that fills the detection window. The Texas A&M University logo has a complicated shape making this more of an imaging case vs simple localization. Due to the size of the source there is nothing to localize if anything, it is the boundaries between regions that are being identified.

This test will show that complex images can be reconstructed and that this can be done with much fewer samples than raster scan. In short, this is the initial feasibility study for the design.

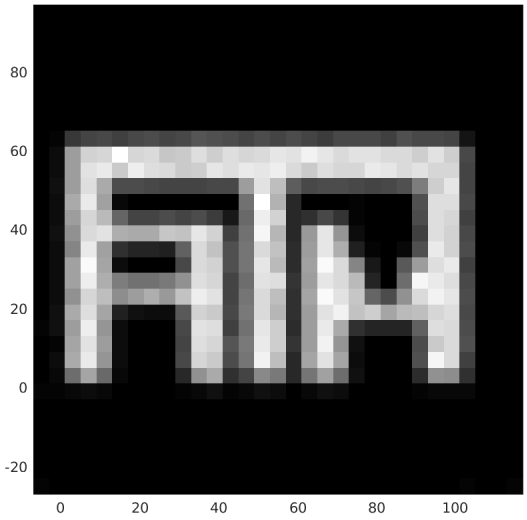

Figure 4.1: The MCNP detector results of the Texas A&M University logo, which are used for sampling.

Figure 4.1 above shows the reference model of the Texas A&M University logo. This is what all the reconstructions are compared to for visual and error analysis. The image has clear delineations between the logo and the background.

Figure 4.2 shows how the various sampling rates performed. Elements of the source structure are visible at as low as 20% while the whole shape is clearly visible at 25%. The improvement continues showing a near perfect reconstruction at 50%. This shows that the collimator design works in rebuilding images and that the sampling rate is much lower than the full pixel count.

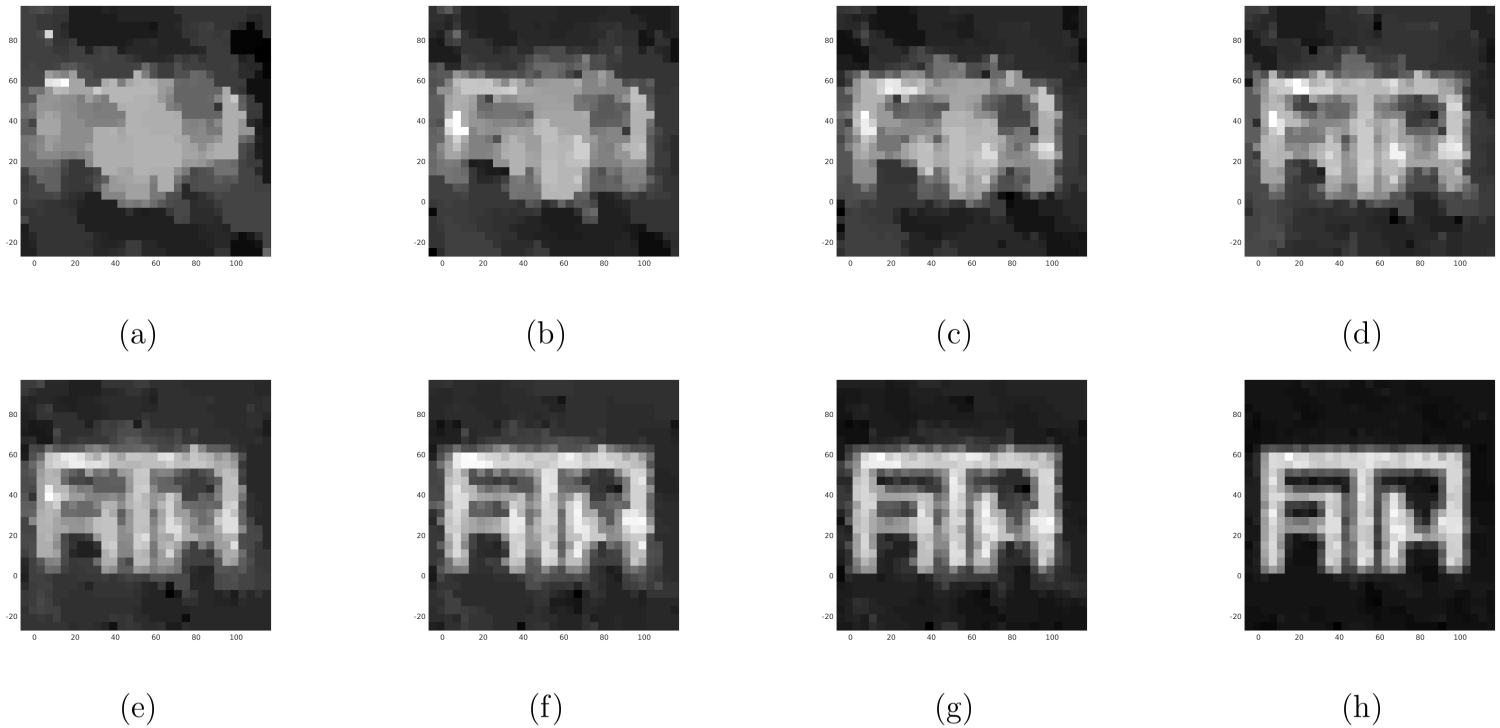

(a) (b) (c) (d)

(e) (f) (g) (h)

Figure 4.2: The reconstructions for the Texas A&M University logo using (a) 10%, (b) 15%, (c) 20%, (d) 25%, (e) 30%, (f) 35%, (g) 40%, and (h) 50% of the pixel count.

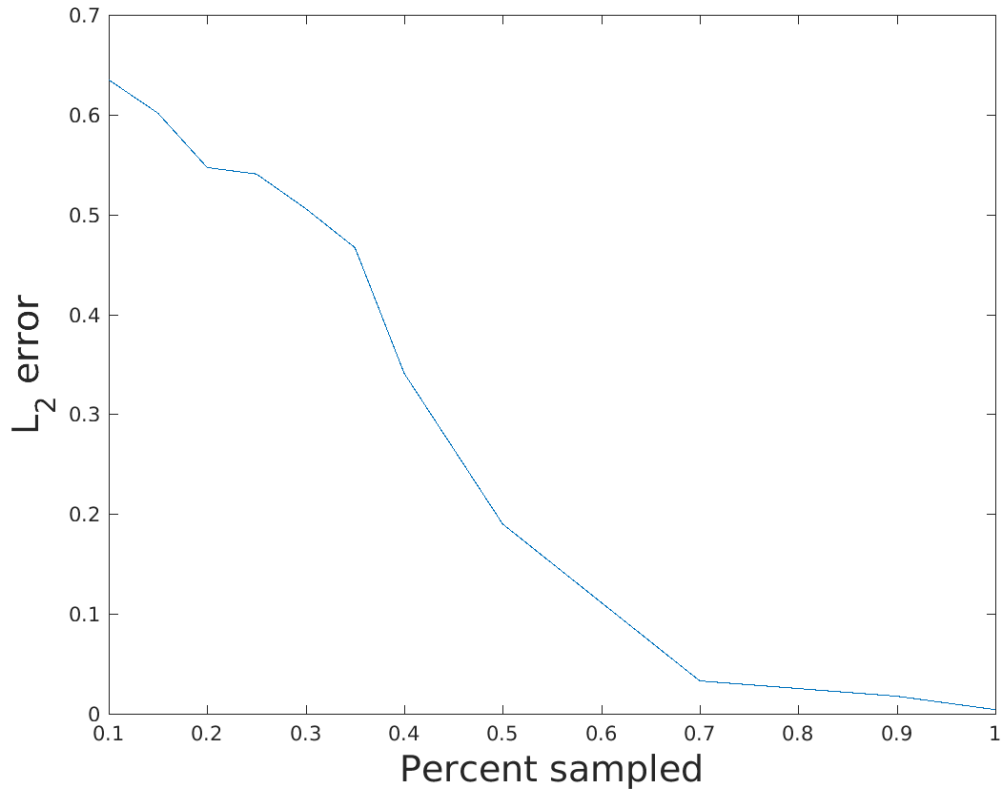

Figure 4.3: The normalized l_2 reconstruction error against sampling percentage.

Figure 4.3 show the l_2 error as the sample size increases. The plot shows that error does not fully drop until sample size is greater the 70%. This displays the property discussed above where the l_2 error remains high but the reconstruction quality is satisfactory. In many cases these levels of l_2 error are not even visible.

The fluctuations in the plot are regions where additional samples increased the sum of the differences squared. This can happen due to the averaging across boundaries. When the images are viewed though, the reconstructions continually improve with sample rate.

4.2 Case 2a

Case 2a involves locating a spherical source located at position $(44, 10)$ in a medium sized cylinder of water. This cylinder is about the size of a common household trashcan. This provides a moderate amount of scattering due to the hydrogen and increases detection difficulty. This is a pure localization problem.

Figure 4.4 show the image being sampled. The is a very simple geometry with small region of pixels with values of larger than zero. This image is very sparse and the goal is to reconstruct it with a small sampling rate.

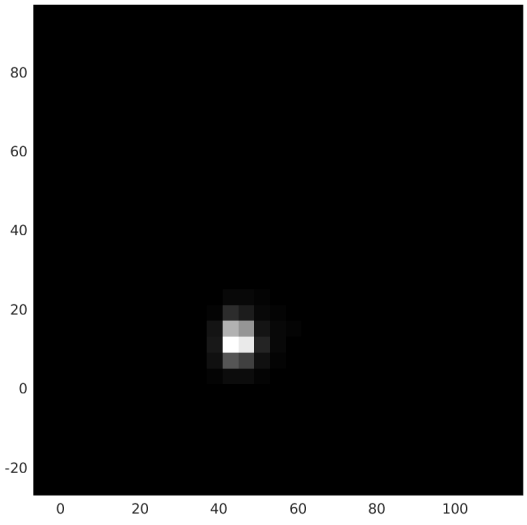

Figure 4.4: The MCNP detector results of the spherical source in cylindrical water container case 2a, which are used for sampling.

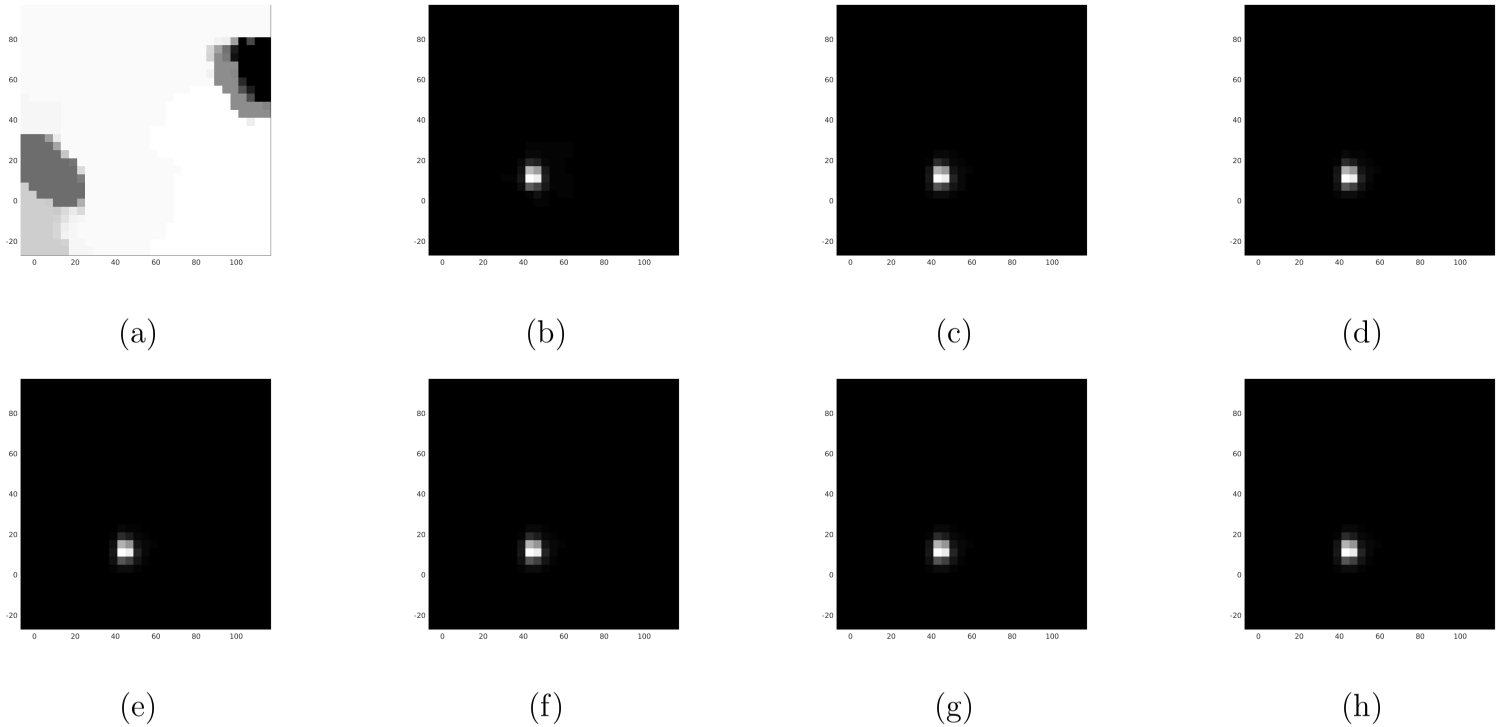

(a) (b) (c) (d)

(e) (f) (g) (h)

Figure 4.5: The reconstructions for the spherical source in a cylindrical water container case 2a using (a) 1%, (b) 5%, (c) 10%, (d) 15%, (e) 20%, (f) 25%, (g) 30%, and (h) 35% of the pixel count.

Figure 4.5 proves that reconstruction with a low sample count is possible. The source is localized with only 5% of the pixel count. Additionally, even though adding more samples improves the error the localization is unchanged. This means that concentrated sources can be accurately identified with a low sample count. This is one of the main uses for this technology.

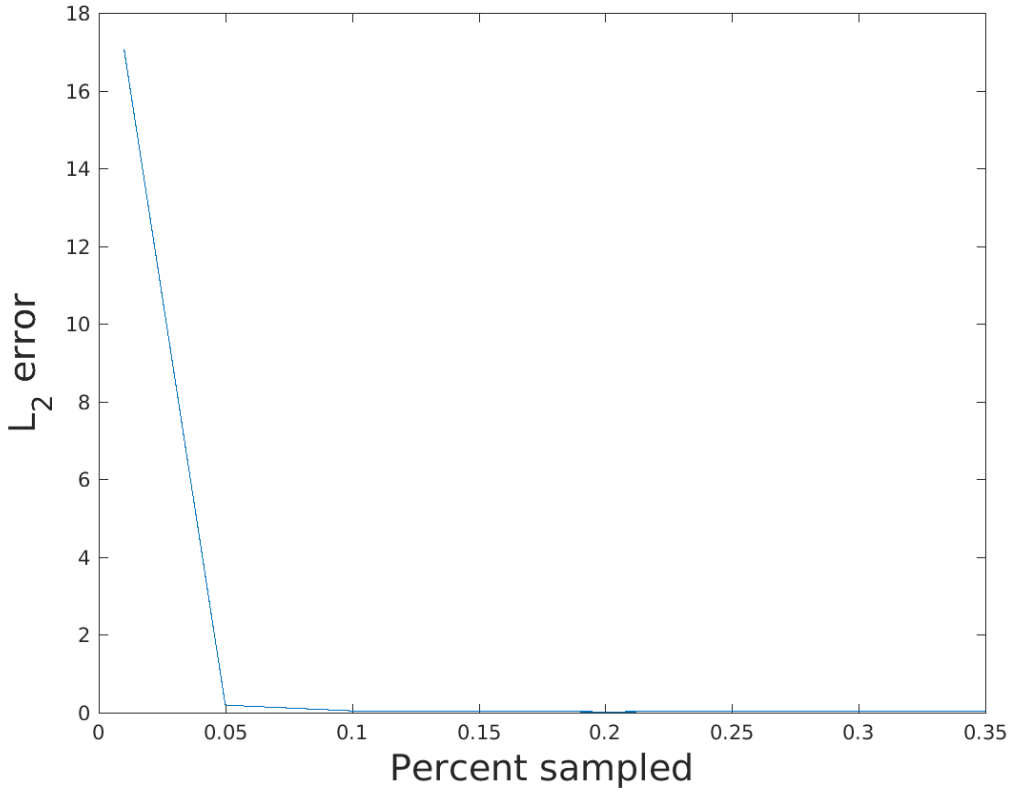

Figure 4.6: The normalized l_2 reconstruction error against sampling percentage.

The l_2 error has a sharp drop off as additional samples are taken. At about 10% the image is perfectly reconstructed. The error in this problem is not the main attribute of interest. Since most of the pixels in the image are 0's, the reconstructions tend to

introduce some low level noise at low sample rates. This significantly affects error while having no affect on localization.

4.2.1 Case 2a with Helium Fill Gas

The various cases were run with helium fill gas instead of air. Case 2 results show the most meaningful deviation with the change in fill gas. This corresponds to the previous discussion, which links low particle count to the need for fill gas.

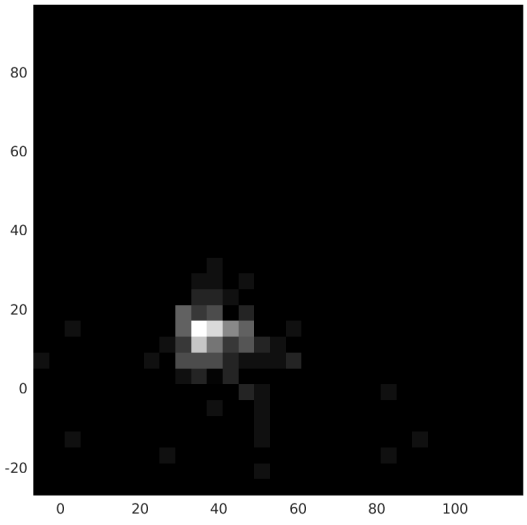

Figure 4.7: The MCNP detector results of the spherical source in cylindrical water container case 2a with helium fill gas, which are used for sampling.

Figure 4.7 shows the image that is detected when air is replaced with helium fill gas. There is an increase in non-zero pixel count relative to Figure 4.4. Additionally, the flux is asymmetric since the source is unevenly shielded. This characteristic cannot be seen in the air filled image.

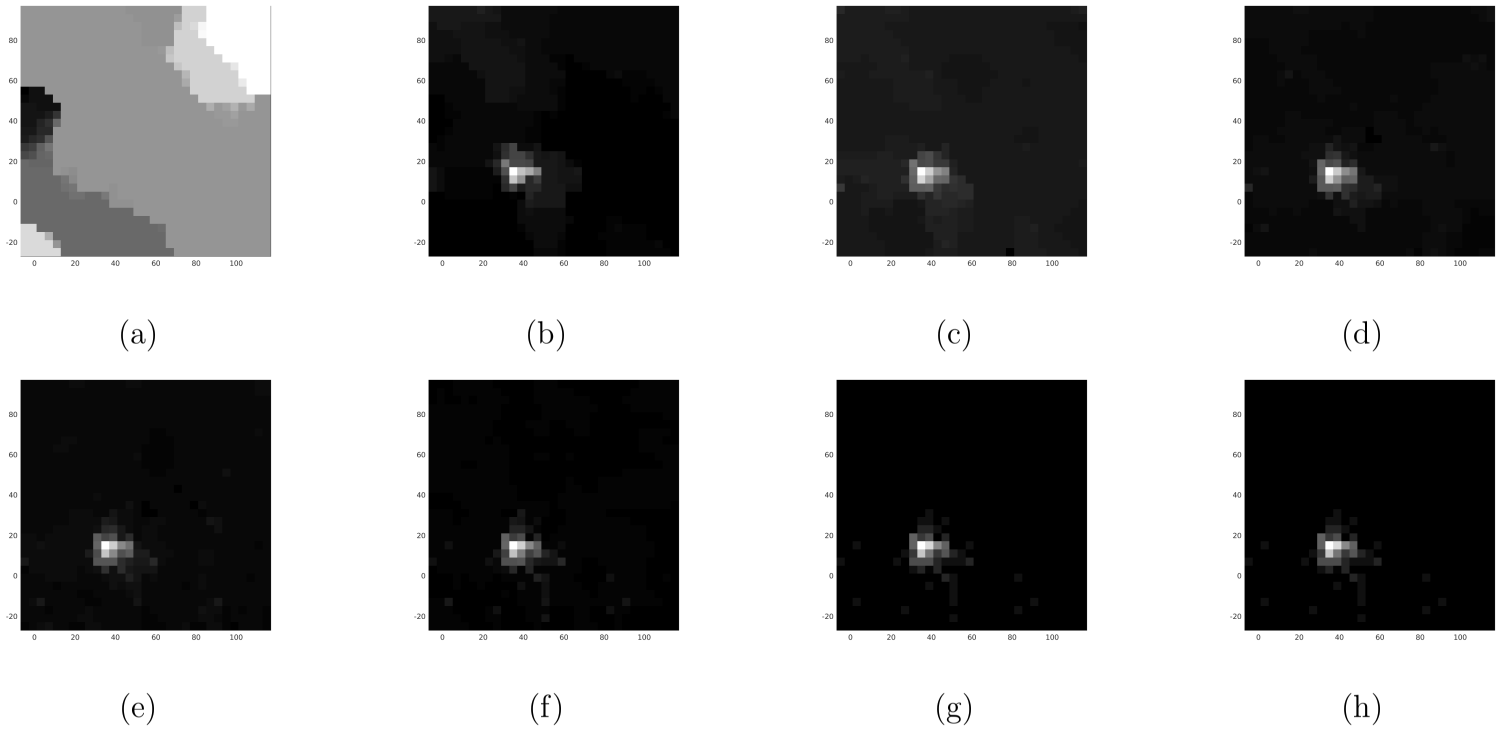

(a) (b) (c) (d)

(e) (f) (g) (h)

Figure 4.8: The reconstructions for the spherical source in a cylindrical water container case 2a with helium using (a) 1%, (b) 5%, (c) 10%, (d) 15%, (e) 20%, (f) 25%, (g) 30%, and (h) 35% of the pixel count.

Figure 4.8 describes the reconstruction quality with a change in sampling rate. At about 5% the source is well reconstructed and localized. This is the same number of samples as the air filled image. The localization of the source is worse because the asymmetry makes the source appear to be shifted. This is expressed by a move to the left in the helium images.

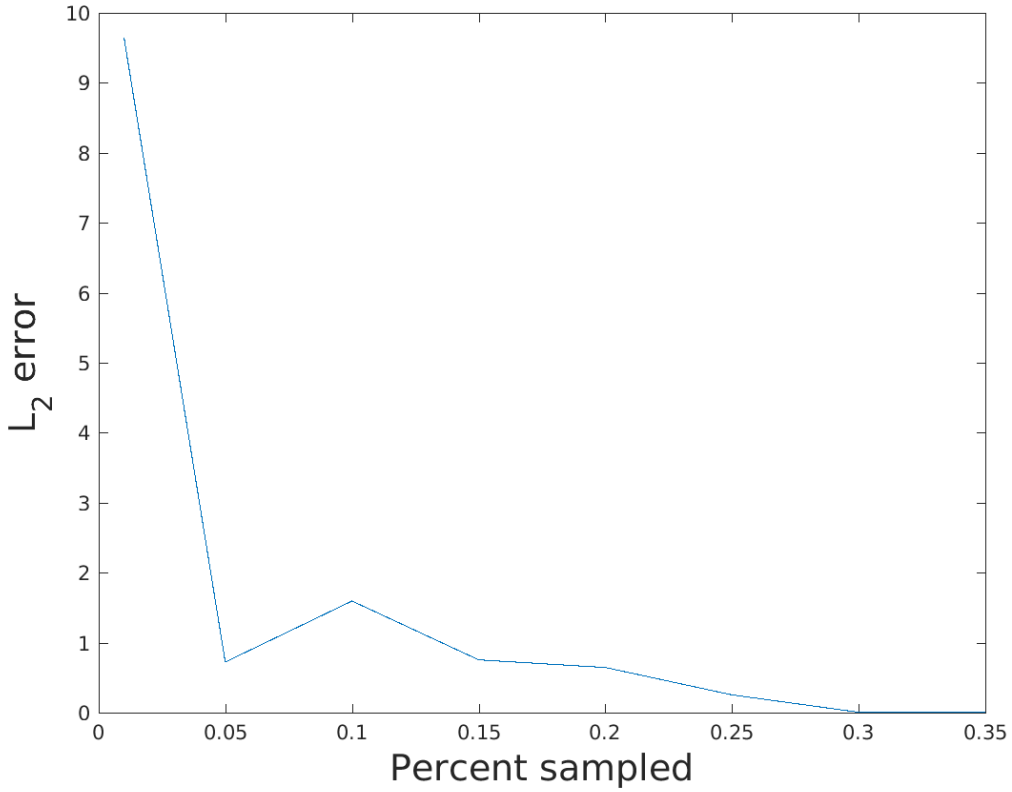

Figure 4.9: The helium fill gas normalized l_2 reconstruction error against sampling percentage.

Figure 4.9 shows that there is an increase in l_2 error against the air filled example. This is seen in the 5% and 10% reconstructions where the error is practically gone for

air but is significant for helium. This is a result of the increased number of non-zero pixels.

4.3 Case 2b

Case 2b is meant to further stress the system by increasing the cylindrical water shielding. Now, the shield is approximately the size of an oil drum. The source is placed along the centerline at $(55, 70)$, which is the position providing maximum shielding when viewed from both sides.

Figure 4.10 show the reference image. This is almost like sampling a delta function since most of the pixel values are zero. This test will determine if identifying a small subset of positive values is possible with a low sampling rate. The concern is a situation where the random map misses the non-zero pixels for too many samples.

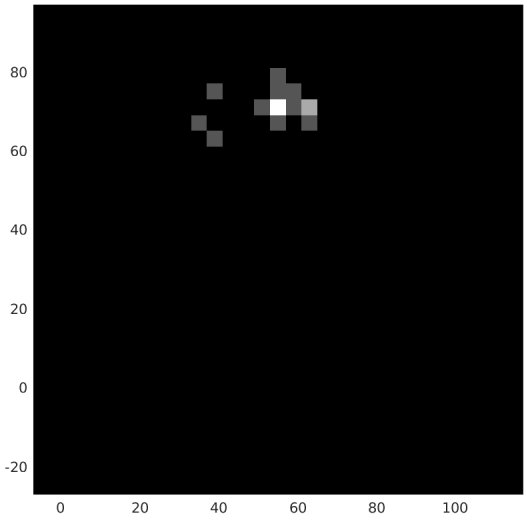

Figure 4.10: The MCNP detector results of the spherical source in cylindrical water container case 2b, which are used for sampling.

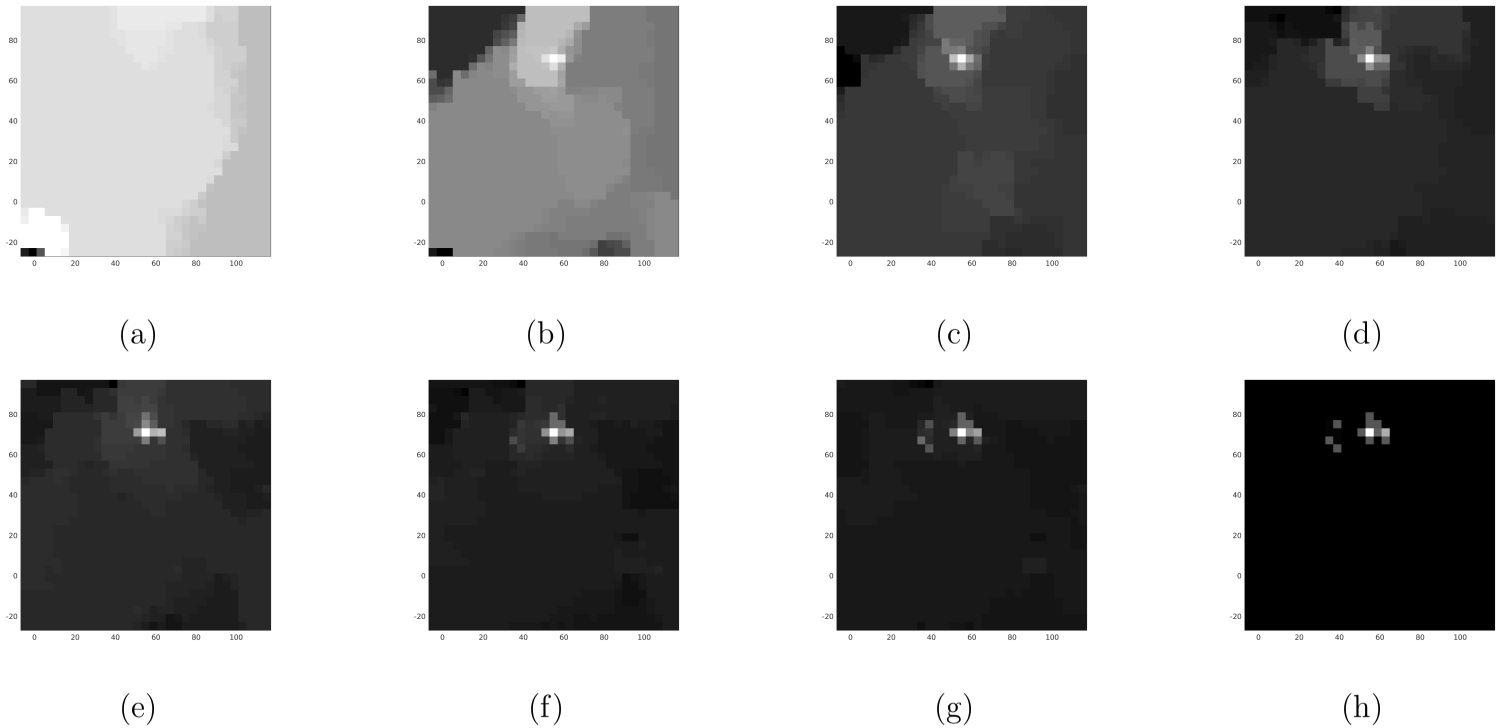

(a) (b) (c) (d)

(e) (f) (g) (h)

Figure 4.11: The reconstructions for the spherical source in a cylindrical water container case 2b using (a) 1%, (b) 2%, (c) 3%, (d) 4%, (e) 5%, (f) 6%, (g) 7%, and (h) 8.5% of the pixel count.

Although the reconstruction quality is slightly worse, Figure 4.11 shows that a sampling rate of 3% is able to clearly localize the source. This is a very important result because it covers the cases of course collimator channels, large distance from the source, and heavier amounts of shielding. In all these cases the image will have most of the pixels with no detection and a small subset with some signal.

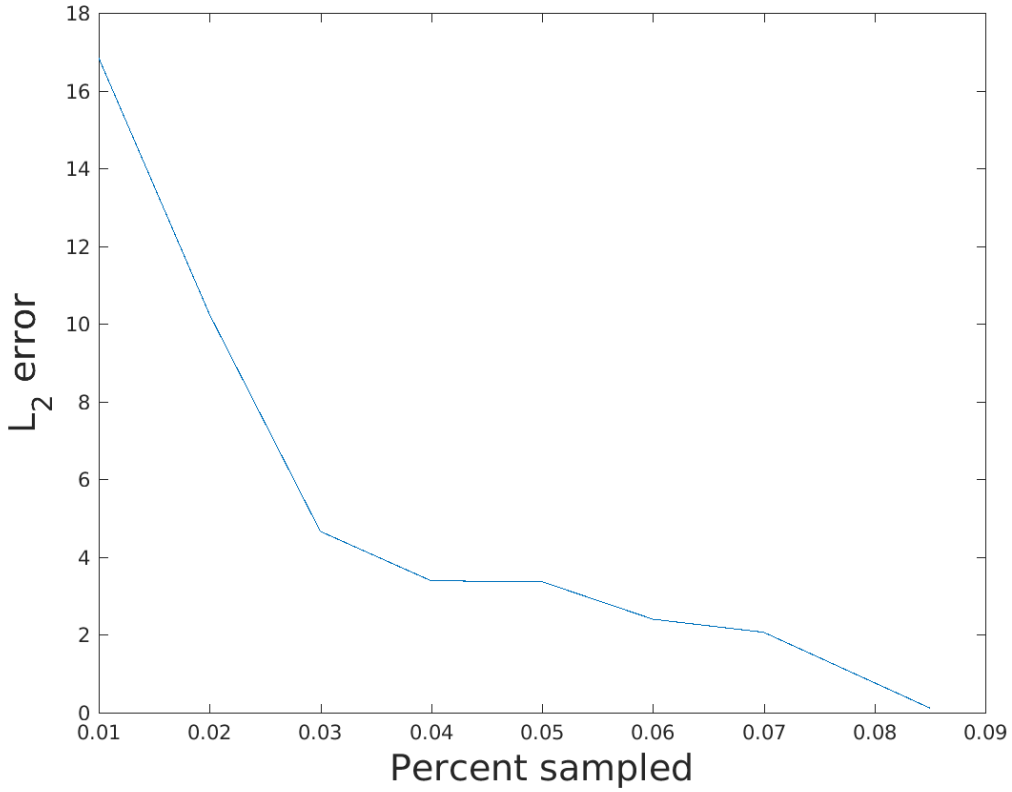

Figure 4.12: The normalized l_2 reconstruction error against sampling percentage.

The l_2 error plot is very similar to case 2a. The values are higher at the beginning because of the delta function like nature of the reference image. The error drops off faster towards the end because the image is sparser than in the previous case.

4.3.1 Case 2b with Helium Fill Gas

Case 2b has the lowest non-zero pixel count of all the tests run. This is primarily because the source is surounded by a large amount of water. The fill gas ends up having very little effect because there are so few particles that penetrate.

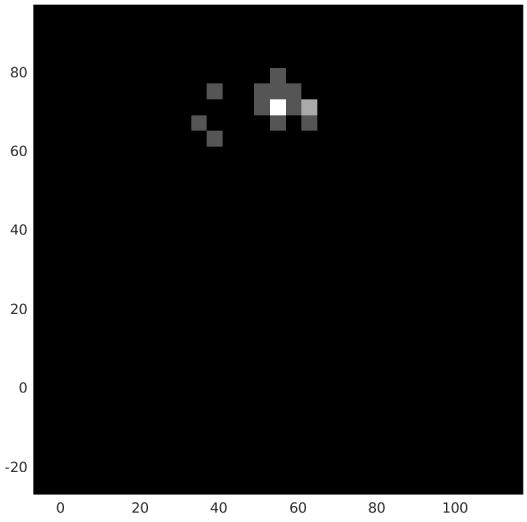

Figure 4.13: The MCNP detector results of the spherical source in cylindrical water container case 2b with helium fill gas, which are used for sampling.

Figure 4.13 shows the image captured by the detector when air is replaced with helium in the collimator channels. There are slightly more non-zero pixels than shown in Figure 4.10.

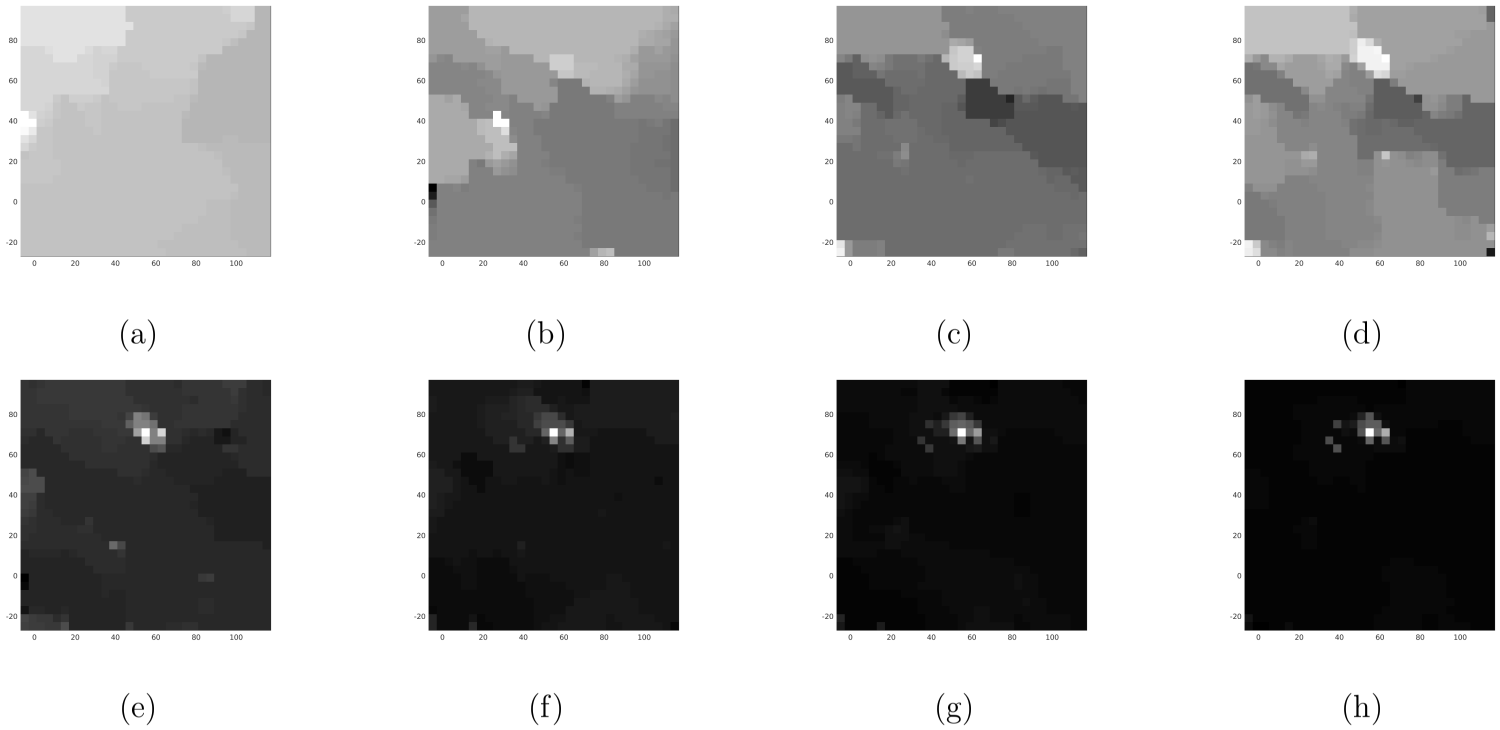

(a) (b) (c) (d)

(e) (f) (g) (h)

Figure 4.14: The reconstructions for the spherical source in a cylindrical water container case 2b using (a) 1%, (b) 2%, (c) 3%, (d) 4%, (e) 5%, (f) 6%, (g) 7%, and (h) 8.5% of the pixel count.

Figure 4.14 shows the reconstructions as the sampling rate is changed. At about 5% the source is well reconstructed and localized. This is slightly more samples than the air filled image. Images with higher non-zero pixel counts generally take more samples to reconstruct but in this case since the difference is relatively small the likelihood is that more samples are required due to the random reconstruction basis.

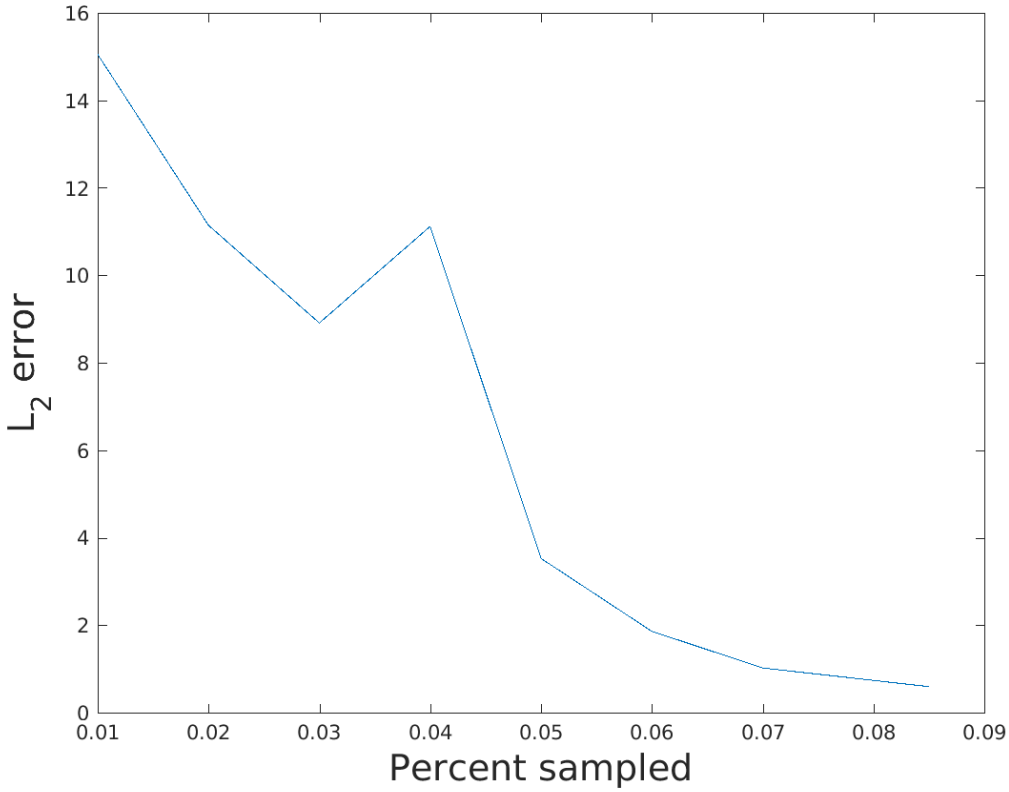

Figure 4.15: The helium fill gas normalized l_2 reconstruction error against sampling percentage.

Figure 4.15 shows that indeed there is an increase in l_2 error against the air filled

example. The concern is that particle count can be so low that some sources are not detected at all. When dealing with very small incident particle counts a helium fill gas should be considered.

4.4 Case 3

Case 3 takes a wide variety of shielding materials and places targets inside for active interrogation. The source directs a perpendicular plane beam through the material to be imaged. The desire is to observe the density variations that will be produced.

The ULD container will have some typical explosive materials and a sphere of weapons grade plutonium. The goal is to distinguish the materials of interest within their respective shields. Also, this problem will measure the ability to reconstruct something with a more complicated geometry.

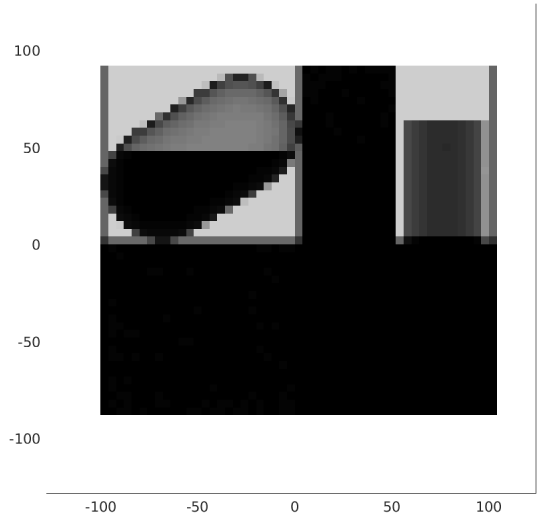

Figure 4.16: The MCNP detector results of the ULD test problem, which are used for sampling.

Figure 4.16 shows the reference image. The cylinderical tank with propane and gasoline is clearly distinguishable. Also, the fertilizer is seen within its container. All three materials have distinct colors meaning that densities can be estimated for these portions of the image. Unfortunately, the flux penetrating the other regions of interest is much lower due to shielding. The image is then viewed in log scale in order to see if finer features can be identified.

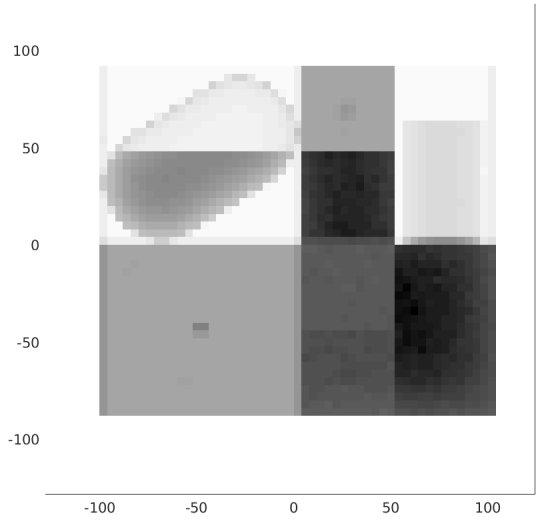

Figure 4.17: The MCNP detector results of the ULD test problem in logarithmic view, which are used for sampling.

Figure 4.17 is able to distinguish some materials in the shielded boxes. The weapons grade plutonium sphere can be seen in the center box around the (-50,-50) position. The contrast between the surrounding material is faint. Also, the TNT is barely visible in the wooden box near the (30,60) position. The other materials are too heavily shielded to be detected.

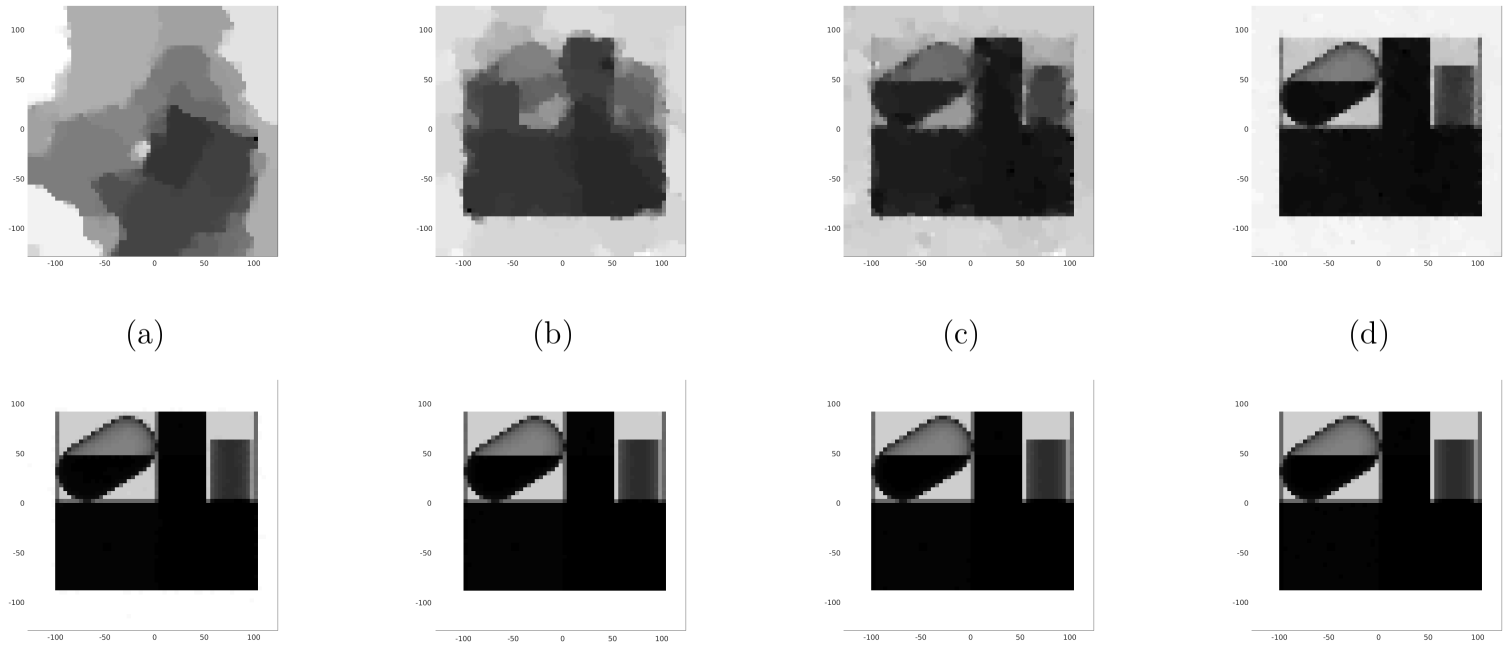

(a) (b) (c) (d)

(e) (f) (g) (h)

Figure 4.18: The reconstructions for the ULD problem using (a) 1%, (b) 5%, (c) 10%, (d) 20%, (e) 30%, (f) 40%, (g) 50%, and (h) 70% of the pixel count.

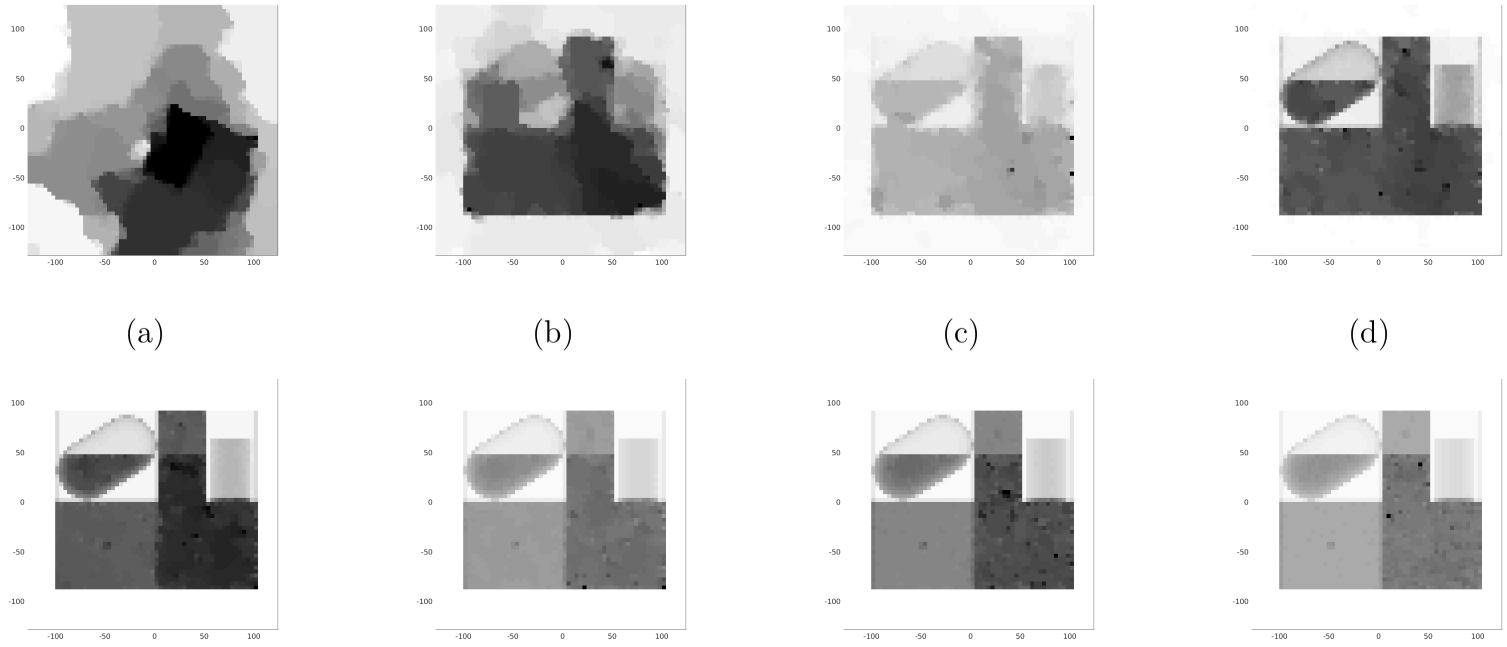

(a) (b) (c) (d)

(e) (f) (g) (h)

Figure 4.19: The logarithmic view of the reconstructions for the ULD problem using (a) 1%, (b) 5%, (c) 10%, (d) 20%, (e) 30%, (f) 40%, (g) 50%, and (h) 70% of the pixel count.

Figures 4.18 and 4.19 show how the reconstructions progress as more samples are increased. As sampling rate goes beyond 20%, the quality is near perfect. This means that everything that was identifiable in the original image is visible in the reconstruction. The log images are slightly less successful. The TNT or weapons grade plutonium only become visible above the 40% sampling mark. This is due to the large differential between the flux through the shielded box and the rest of the ULD. The hope is to fix this by zooming the collimator once shielded volumes are identified, The collimator can 'zoom' in on that portion by shutting all the flaps that are not pointing at the region of interest.

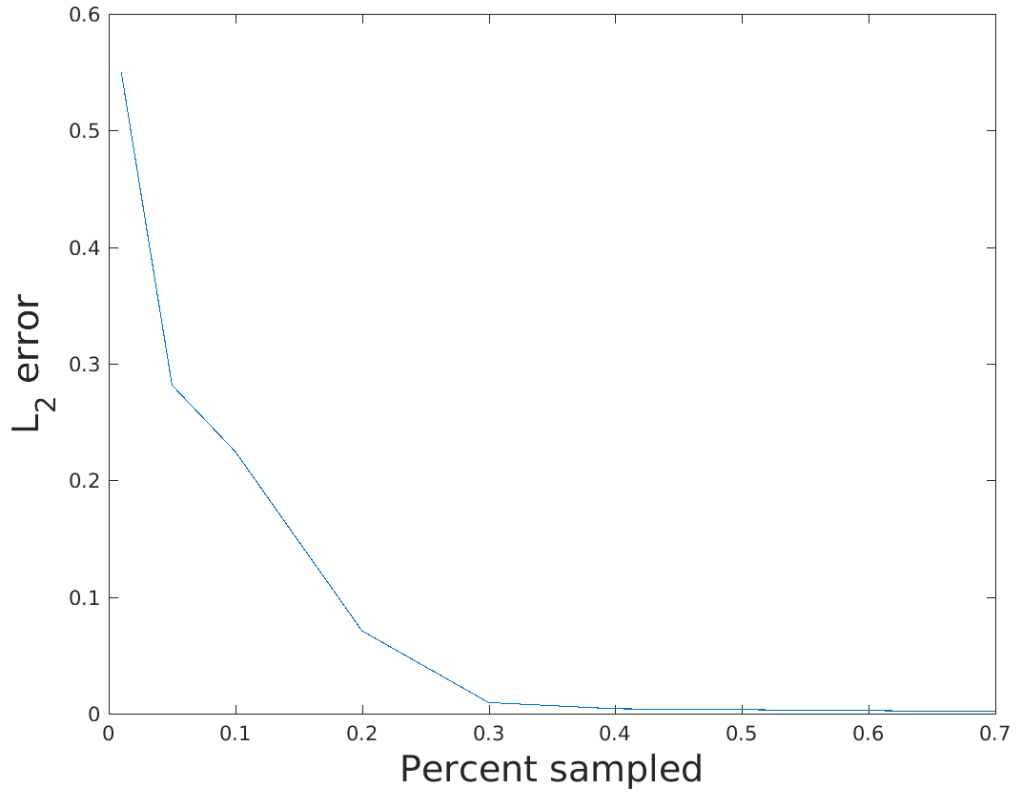

Figure 4.20: The normalized l_2 reconstruction error against sampling percentage.

Figure 4.20 shows the decay the l_2 with increased sampling. The error decays smoothly and is negligible around 30%. It seems that as the image complexity increases the drop off in error is smoother and the visual reconstruction matches the l_2 plots better. Still it seems that to measure complicated images with decades difference in results, the collimator needs many samples and problem regions require refocusing and additional imaging.

5. CONCLUSION AND FUTURE WORK

The testing of the compressive sensing based single pixel neutron detector has shown that there are many benefits and applications to this sort of setup. This design is simple and therefore can be implanted without expense. This becomes especially pertinent when scaling this system for large portals and reproducing it in multiple locations. Localization of the sources can be done quickly meaning that materials of interest can be identified in large volumes so that further study can be performed. Detector efficiency can be significantly increased since the detector volume is no longer tied to image resolution. The overall shift for this type of product is away from detector design and toward creative implementations of a collimator.

The goal of this project was to create an inexpensive and simple imaging system for localizing neutron sources. The compressive sensing based single pixel neutron detector accomplishes both of these goals. The design only requires a collimator attachment and can function with any detector available. This is a technology that is especially applicable to multiplexing systems since it will produce similar quality results with much fewer samples. The simplicity of the design makes it easily reconfigurable to any situation. The collimator length can be adjusted, the material composition can be modified, and the channel shape can changed all to meet design needs. The general idea of allowing random maps of neutron streams has many possible implementations.

Localization of sources can be accomplished with remarkably few samples. As shown in the results, sample rates of as low as 5% were able to identify the position of the

source even with significant amounts of shielding. Although more complicated images require ever increasing sampling rates, this system can quickly give an estimate location with some information regarding the source shape and surrounding shielding.

This approach has benefits for sources with low emission rates. If there are few particles to detect it becomes important to measure all the ones that enter the detector area. Since in many cases the detector efficiency will be strongly affected by material properties, the one parameter that can be changed to increase efficiency is detector volume. Of course, increasing volume will reduce the resolution in a standard array system. This is not the case in the single pixel setup since the collimator controls resolution.

The design of a detector can be complicated by material and size considerations. The amount of materials used in constructing a detector is much larger than those used in the collimator. The neutron particle is opaque to many types of interactions making it difficult to measure in a small detector volume. Additionally, nearby detectors can detect off-angle neutrons creating blur. Focusing on the collimator may allow for a solution to problems that required resolutions or energy ranges which are difficult to measure with an array of detectors. For these reasons, moving the design considerations toward the collimator can simplify the overall detection system while increasing the useful range to additional problems.

5.1 Future Work

The ability to restore signals from a limited sample can be expanded into two new areas: resolving particle energies and 3D reconstruction. The resolution of energies is important in identifying the composition of the material being measured. Specific

energies are keyed to certain materials so identifying the neutron energy spectrum can be used to determine the material makeup. Another interesting area is 3D model reconstruction. Multiple images can be used to estimate a higher dimensional model through minimization. These areas will further the ability to interrogate volumes for constituents of interest.

The ability to reconstruct energy distributions is problematic since detectors have a difficult time differentiating between particle energies and since higher energy particles have a lower likelihood of being detected. This difficulty can be overcome by resolving energies using the same principles from 2D reconstruction. A inner product would be taken of the energy distribution and a random map supplying the samples used to rebuild the full distribution. The random mapping can be accomplished by placing shields that have designed material compositions and thickness, which block select energies. Only a random set of energies would be allowed to pass, the sum of which becomes the measurement. With the set of measurements and the random map composed of shield combinations, the full distribution can be reconstructed. This method has promise as long as the distribution is smooth and can be represented in a sparse basis.

The other possible expansion is to take the various measurements to build higher dimensional models. Compressive sensing has been used to rebuild a three-dimensional model from two-dimensional projections using optimization algorithms. The methodology is different than what was used above. These problems use background-subtracted silhouettes to solve multi-view estimation problems, which allow multiple 2D views of the same object to be reconstructed into a 3D model.

This technology has many possible implementations and is very versatile in sense that it is easily adaptable to many problem types. The design in this paper allows for simple and yet affective interrogation. More sophisticated designs can be built to optimize toward the properties being measured and the constraints imposed by the problem. These designs and the advancements allowed through the field of compressive sensing are greatly needed as demand for superior interrogation systems increases in the future.

REFERENCES

[1] J. M. Hall, S. Asztalos, P. Biltoft, J. Church, M.-A. Descalle, T. Luu, D. Manatt, G. Mauger, E. Norman, D. Petersen, et al., The nuclear car wash: Neutron interrogation of cargo containers to detect hidden snm, Nuclear Instruments and Methods in Physics Research Section B: Beam Interactions with Materials and Atoms 261 (1) (2007) 337–340.

[2] E. H. Lehmann, P. Vontobel, G. Frei, C. Brönnimann, Neutron imagingdetector options and practical results, Nuclear Instruments and Methods in Physics Research Section A: Accelerators, Spectrometers, Detectors and Associated Equipment 531 (1) (2004) 228–237.

[3] E. Lehmann, Status of neutron imaging, in: Lasers and Nuclei, Springer, 2006, pp. 231–249.

[4] M. F. Duarte, Y. C. Eldar, Structured compressed sensing: From theory to applications, Signal Processing, IEEE Transactions on 59 (9) (2011) 4053–4085.

[5] M. F. Duarte, M. A. Davenport, D. Takhar, J. N. Laska, T. Sun, K. E. Kelly, R. G. Baraniuk, et al., Single-pixel imaging via compressive sampling, IEEE Signal Processing Magazine 25 (2) (2008) 83.

[6] R. Baraniuk, M. A. Davenport, M. F. Duarte, C. Hegde, An introduction to compressive sensing, Connexions e-textbook.

[7] E. Candes, T. Tao, The dantzig selector: statistical estimation when p is much larger than n, The Annals of Statistics (2007) 2313–2351.

[8] E. Candes, J. Romberg, Sparsity and incoherence in compressive sampling, Inverse problems 23 (3) (2007) 969.

[9] S. Boyd, L. Vandenberghe, Convex optimization, Cambridge university press, 2004.

[10] E. Candes, J. Romberg, l1-magic: Recovery of sparse signals via convex programming, URL: www. acm. caltech. edu/l1magic/downloads/l1magic. pdf 4 (2005) 14.

[11] R. T. Kouzes, E. R. Siciliano, J. H. Ely, P. E. Keller, R. J. McConn, Passive neutron detection for interdiction of nuclear material at borders, Nuclear Instruments and Methods in Physics Research Section A: Accelerators, Spectrometers, Detectors and Associated Equipment 584 (2) (2008) 383–400.

[12] J. Jones, W. Yoon, D. Norman, K. Haskell, J. Zabriskie, S. Watson, J. Sterbentz, Photonuclear-based, nuclear material detection system for cargo containers, Nuclear Instruments and Methods in Physics Research Section B: Beam Interactions with Materials and Atoms 241 (1) (2005) 770–776.

[13] J. Eberhardt, S. Rainey, R. Stevens, B. Sowerby, J. Tickner, Fast neutron radiography scanner for the detection of contraband in air cargo containers, Applied Radiation and Isotopes 63 (2) (2005) 179–188.

[14] G. MacGillivray, Neutron radiography collimator design, Nray Services Inc.

APPENDIX A

SAMPLE MCNP SCRIPT

```
 Cargo Container with collimator and shield
c ******************** BLOCK 1: CELL CARDS ****************************
c This is the collimator box
    1     0         1 -2 3 -4 5 -6 fill=1 IMP:N=1 IMP:P,E,H=0
c Lattice
    2     0         7 -8 9 -10 11 -12 u=1 fill=2 lat=1 IMP:N=1 IMP:P,E,H=0
c Hole
    3     4 -0.000166         13 -14 15 -16 17 -18 u=2 IMP:N=1 IMP:P,E,H=0
    4     20 -18.13         (-13:14:-15:16:-17:18) u=2 IMP:N=1 IMP:P,E,H=0
c This is the extra shielding
    5     20 -18.13         19 -20 IMP:N=1 IMP:P,E,H=0 $ Borated Poly
c This is the Detector shield
    6     20 -18.13         -21 IMP:N=1 IMP:P,E,H=0 $ Borated Poly
c This is the back shield
    7     4 -0.000166         -22 IMP:N=1 IMP:P,E,H=0
c This is the front shield
    8     4 -0.000166         -23 IMP:N=1 IMP:P,E,H=0
c This is the Detector
    9     4 -0.000166         -24 IMP:N=1 IMP:P,E,H=0
c This is the detector void
   10     0            -25 IMP:N=0 IMP:P,E,H=0
c This is the ULD
   11     9 -2.6989            26 -27 IMP:N=1 IMP:P,E,H=0
```

```
c This is the mix cylinder housing (steel)
   12     8 -7.92            44 45 46 (-28:-29:-30) IMP:N=1 IMP:P,E,H=0
c This is the mix cylinder liquid (gasoline)
   13     10 -0.6837            -47 (-44:-45:-46) IMP:N=1 IMP:P,E,H=0
c This is the mix cylinder gas (propane)
   14     18 -0.00187939            47 (-44:-45:-46) IMP:N=1 IMP:P,E,H=0
c This is the large box (wood + wgpu)
   15     7 -0.593            32 -31 IMP:N=1 IMP:P,E,H=0
   16     6 -19.84            -32 IMP:N=1 IMP:P,E,H=0
c This is the small box 1 (wood + tnt)
   17     7 -0.593            34 -33 IMP:N=1 IMP:P,E,H=0
   18     12 -1.654            -34 IMP:N=1 IMP:P,E,H=0
c This is the small box 2  (steel + rdx)
   19     8 -7.92            36 -35 IMP:N=1 IMP:P,E,H=0
   20     13 -1.806            -36 IMP:N=1 IMP:P,E,H=0
c This is the small box 3 (pvc + nitro)
   21     19 -1.406            38 -37 IMP:N=1 IMP:P,E,H=0
   22     15 -1.13            -38 IMP:N=1 IMP:P,E,H=0
c This is the small box 4 (al + water + ammonium nitrate)
   23     9 -2.6989            48 -39 IMP:N=1 IMP:P,E,H=0
   24     5 -1            40 -48 IMP:N=1 IMP:P,E,H=0
   25     17 -1.730            -40 IMP:N=1 IMP:P,E,H=0
c This is the medium box
   26     8 -7.92            -41 IMP:N=1 IMP:P,E,H=0
c This is the fert cylinder
   27     9 -2.6989            42 -43 IMP:N=1 IMP:P,E,H=0
   28     11 -0.990            -42 IMP:N=1 IMP:P,E,H=0
```

```
c This is the surrounding region in the ULD
   98     1 -0.001205         28 4I 33 35 3I 43 -26 IMP:N=1 IMP:P,E,H=0
c This is the surrounding region
   99     1 -0.001205         20 27 -100 IMP:N=1 IMP:P,E,H=0
c This is the blackhole
  100     0          100 IMP:N,P,E,H=0


c ********************* BLOCK 2: SURFACE CARDS ************************
c Outer Lattice
    1        px -130
    2        px 126
    3        py 520
    4        py 720
    5        pz -130
    6        pz 126
c Small box
    7        px -2
    8        px 2
    9        py 520
   10        py 720
   11        pz -2
   12        pz 2
c Hole
   13        px -1
   14        px 1
   15        py 520
   16        py 720
```

```
   17        pz -1
   18        pz 1
c This is the collimator box 1
   19        box -130 518 -130 256 0 0 0 212 0 0 0 256
c This is the collimator box 2
   20        box -150 518 -150 296 0 0 0 212 0 0 0 296
c This is the detector shield
   21        box -130 726 -130 256 0 0 0 4 0 0 0 256
c This is the back shield
   22        box -130 720 -130 256 0 0 0 2 0 0 0 256
c This is the front shield
   23        box -130 518 -130 256 0 0 0 2 0 0 0 256
c This is the detector
   24        box -130 722 -130 256 0 0 0 2 0 0 0 256
c This is the absorption void
   25        box -130 724 -130 256 0 0 0 2 0 0 0 256
c This is inner ULD
   26        box -100 315 -90 200 0 0 0 160 0 0 0 180
c This is outer ULD
   27        box -101 314 -91 202 0 0 0 162 0 0 0 182
c Gas/Liquid Cyl outer
   28        rcc -70 395 30 40 0 25 30
   29        sph -70 395 30 30
   30        sph -30 395 55 30
c Gas/Liquid Cyl inner
   44        rcc -70 395 30 40 0 25 29
   45        sph -70 395 30 29
```

```
   46        sph -30 395 55 29
   47        box -100 315 0 100 0 0 0 160 0 0 0 45
c This is large box
   31        box -100 355 -90 100 0 0 0 80 0 0 0 90
   32        sph -50 395 -45 4
c This is small box 1
   33        box 0 355 45 50 0 0 0 80 0 0 0 45
   34        sph 25 395 67 5
c This is small box 2
   35        box 0 355 0 50 0 0 0 80 0 0 0 45
   36        sph 25 395 22 5
c This is small box 3
   37        box 0 355 -45 50 0 0 0 80 0 0 0 45
   38        sph 25 395 -23 5
c This is small box 4
   39        box 0 355 -90 50 0 0 0 80 0 0 0 45
   48        box 1 356 -89 48 0 0 0 78 0 0 0 43
   40        sph 25 395 -68 5
c This is medium box
   41        box 50 355 -90 50 0 0 0 80 0 0 0 90
c This is fert container
   42        rcc 75 395 1 0 0 60 20
   43        rcc 75 395 0 0 0 62 21
c This is the universe
  100        box -330 200 -330 660 0 0 0 620 0 0 0 660

c ********************* BLOCK 3: DATA CARDS ****************************
```

```
MODE N
PHYS:n 15.0 0.1
NPS 10e9
CUT:N j 0.01
c
c --- Building Materials
c Density = -0.001205
m1 & $ Air (C:-0.000124, N:-0.755268, O:-0.231781, Ar:-0.012827) [NIST]
6000.80c -0.000124 &
7014.80c -0.755268 &
8016.80c -0.231781 &
18040.80c -0.012827
m2 & $ Borated polyethylene
6000.80c -0.774645 &
1001.80c -0.125355 &
5010.80c -0.1
m3 & $ Boron carbide rho=2.52
5011.80c -0.782610 &
6000.80c -0.217390
m4 & $ Helium gas rho=0.000166
2004.80c -1
m5 & $ water rho=1
1001.80c 0.6665667 &
1002.80c 0.000100 &
8016.80c 0.3332063 &
8017.80c 0.000127
mt5 lwtr.60t
```

```
m6 & $ WGPu, DOE 3013, rho = 19.84
94238.80c -0.000500 &
94239.80c -0.935000 &
94240.80c -0.060000 &
94241.80c -0.004000 &
94242.80c -0.000500
m7 & $ wood rho=0.593
1001.80c -0.057889 &
6012.42c -0.482667 &
8016.80c -0.459444
m8 & $ steel 316 rho=7.92
14000.42c -0.010 &
24000.42c -0.170 &
25055.80c -0.020 &
26000.42c -0.655 &
28000.42c -0.120 &
42000.42c -0.025
m9 & $ aluminum rho=2.6989
13027.80c -1
m10 & $ gasoline rho=0.6837
1001.80c -0.16 &
6012.42c -0.84
m11 & $ fertilizer rho=0.990
1001.80c -0.0000504 &
8016.80c -0.0007176 &
11023.80c -0.0087350 &
12000.62c -0.0002058 &
```

```
16000.62c -0.0001590 &
17000.42c -0.4778000 &
19000.62c -0.5117000 &
20000.62c -0.0002758 &
35079.80c -0.0003303
m12 & $ tnt rho=1.654
1001.80c -0.022189 &
6012.42c -0.370160 &
7014.80c -0.185004 &
8016.80c -0.422648
m13 & $ rdx rho=1.806
1001.80c -0.027227 &
6012.42c -0.162222 &
7014.80c -0.378361 &
8016.80c -0.432190
m14 & $ hmx rho=1.902
1001.80c -0.027227 &
6012.42c -0.162222 &
7014.80c -0.378361 &
8016.80c -0.432190
m15 & $ nitro rho=1.13
1001.80c -0.022193 &
6012.42c -0.158671 &
7014.80c -0.185040 &
8016.80c -0.634096
m16 & $ petn rho=1.773
1001.80c -0.025506 &
```

```
6012.42c -0.189961 &
7014.80c -0.177223 &
8016.80c -0.607310
m17 & $ ammonium nitrate rho=1.730
1001.80c -0.050370 &
7014.80c -0.349978 &
8016.80c -0.599652
m18 & $ propane rho=0.00187939
1001.80c -0.182855 &
6012.42c -0.817145
m19 & $ pvc rho=1.406
1001.80c -0.048382 &
6012.42c -0.384361 &
17000.42c -0.567257
m20 & $ densalloy rho=18.13
26000.42c 0.015 &
28000.42c 0.035 &
74000.21c 0.95
c
c --- rectangular plane source perpendicular to the y-axis.
c
SDEF POS=0 310 0 X=d1 Y=310 Z=d2 PAR=1 ERG=14
     VEC=0 1 0 DIR=1
SI1 -130 126
SP1 0 1
SI2 -130 126
SP2 0 1
```

```
c
FMESH14:n   GEOM=XYZ ORIGIN=-129 719 -129
            IMESH= 125 IINTS= 127
            JMESH= 721 JINTS= 1
            KMESH= 125 KINTS= 127
FMESH24:n   GEOM=XYZ ORIGIN=-129 517 -129
            IMESH= 125 IINTS= 127
            JMESH= 519 JINTS= 1
            KMESH= 125 KINTS= 127
PRINT 128
```

APPENDIX B

MATLAB RECONSTRUCTION SCRIPT

```
%%%%%%%%%%%%%%%%%%%%%%%%%%%%%%%%%%%%%%%%%%%%%%%%%%%%%%%%%%%%%%%%%%%%%%%%%%%%
% This Script will allow for the simulation of single pixel imaging by
% creating the test functions, computing the inner product, and
% reconstructing the image
%%%%%%%%%%%%%%%%%%%%%%%%%%%%%%%%%%%%%%%%%%%%%%%%%%%%%%%%%%%%%%%%%%%%%%%%%%%%

path(path, './Functions');
path(path, './DTCWT');
path(path, './Wave2D');

filt = 0;
% Resize original image
tmp_mesh=det1./max(max(det1));
y2=tmp_mesh(1:2:127,1:2:127);
rest=tmp_mesh; rest(1:2:127,1:2:127)=0;

in1=-128:4:124; in2=-128:4:124;
figure;pcolor(in1, in2, y2); colormap(gray),axis image; caxis([0 1]); shading('flat')
figure;pcolor(in1, in2, log(y2)); colormap(gray),axis image; shading('flat')

% Generate the test functions using psuedorandom number generator with
% time seed and Mersenne Twister Number Generator
rng('shuffle', 'twister');
w=64; l=64;
test_fun=round(double(rand(w,l,w*l)));

cnt1=1;
% Sampling percentage
samples = [0.01, 0.05, 0.1, 0.2, 0.3, 0.4, 0.5, 0.7];
for subrate = samples

    % Number of sample points
    w=64; l=64;
```

```
m=round(w*l*subrate);

% Create compression vector
y=squeeze(zeros(m,1));

% Set photodiode efficiency
n=1;

offset=0; %sum(sum(rest));
tmp=zeros(64,64);
for i=1:m
    tmp=y2.*test_fun(:,:,i);

    % Compute the inner product
    y(i) = n*(sum(sum(tmp))+offset);
end

phi=zeros(l*w,m);

for k=1:m
    z=1;
    for i=1:w
        for j=1:l
            phi(k,z)=test_fun(i,j,k);
            z=z+1;
        end
    end
end

phi=phi(1:m,:);

% Optimization parameters
epsilon = 0.01;

% Set initial solution and run TV minimizer
% Output is in column format, raster scan of reconstructed image
% Initial point: minimum energy
x0 = phi\y;
estIm = tvqc_logbarrier(x0, phi, [], y, epsilon,1e-4,2);
```

```
    % Reshape output; flip upside down
    xtvqc = reshape(estIm,sqrt(w^2),sqrt(l^2));
    xtvqc = flipud(xtvqc);

    % Normalize output
    xtvqc = (xtvqc-min(min(xtvqc)))/(max(max(xtvqc))-min(min(xtvqc)));

    tmp_mesh2=xtvqc;
    if filt
        thresh=7e-2; stages=3;
        tmp_mesh2=denC2D(tmp_mesh2,thresh,stages);
        tmp_mesh2=(tmp_mesh2-min(min(tmp_mesh2)))/(max(max(tmp_mesh2))-min(min(tmp_mesh2)));
    end

    l2(cnt1) = sum(sum((y2-imrotate(tmp_mesh2,-90)).^2)).^.5/sum(sum((y2).^2)).^.5;
    cnt1 = cnt1+1;
    % Show reconstruction
    name1 = sprintf('p3_recons_%d.fig', subrate);
    name2 = sprintf('p3_recons_log_%d.fig', subrate);
    name3 = sprintf('p3_recons_%d.png', subrate);
    name4 = sprintf('p3_recons_log_%d.png', subrate);
    h = pcolor(in1, in2, imrotate(tmp_mesh2,-90)),colormap(gray),axis image; shading('flat')
    saveas(h, name1)
    saveas(h, name3)
    h = pcolor(in1, in2, log(imrotate(tmp_mesh2,-90))),colormap(gray),axis image; shading('flat')
    saveas(h, name2)
    saveas(h, name4)
end

% Show the L2 error
name1 = sprintf('p3_recons_l2error.fig');
name2 = sprintf('p3_recons_l2error.png');

figure; h= plot(samples, l2); xlabel('Percent sampled','fontsize',18); ylabel('L_2 error','fontsize',18)

saveas(h, name1)
saveas(h, name2)
```